

# A particle formulation for treating differential diffusion in filtered density function methods

R. McDermott \*, S.B. Pope

*Sibley School of Mechanical and Aerospace Engineering, Cornell University, Ithaca, NY 14853, USA*

Received 5 January 2007; accepted 2 May 2007

Available online 13 May 2007

---

## Abstract

We present a new approach for treating molecular diffusion in filtered density function (FDF) methods for modeling turbulent reacting flows. The diffusion term accounts for molecular *transport* in physical space and molecular *mixing* in composition space. Conventionally, the FDF is represented by an ensemble of particles and transport is modeled by a random walk in physical space. There are two significant shortcomings in this transport model: (1) the resulting composition variance equation contains a spurious production term and (2) because the random walk is governed by a single diffusion coefficient, the formulation cannot account for differential diffusion, which can have a first-order effect in reacting flows. In our new approach transport is simply modeled by a mean drift in the particle composition equation. The resulting variance equation contains no spurious production term and differential diffusion is treated easily. Hence, the new formulation reduces to a direct numerical simulation (DNS) in the limit of vanishing filter width, a desirable property of any large-eddy simulation (LES) approach. We use the IEM model for mixing. It is shown that there is a lower bound on the specified mixing rate such that the boundedness of the compositions is ensured. We present a numerical method for solving the particle equations which is second-order accurate in space and time, obeys detailed conservation, enforces the realizability and boundedness constraints and is unconditionally stable.

© 2007 Elsevier Inc. All rights reserved.

*PACS:* 65C20; 76F65

*Keywords:* Particle method; Differential diffusion; Filtered density function methods; Large-eddy simulation; Direct numerical simulation; Turbulent reacting flow

---

## 1. Introduction

We are interested in modeling chemically reacting turbulent flows, e.g. combustion. This task is complicated in large part due to the nature of turbulence/chemistry interactions, which tend to be highly

---

\* Corresponding author. Current address: Building and Fire Research Laboratory, National Institute of Standards and Technology, 100 Bureau Drive, Mail Stop 8663, Gaithersburg, MD 20899-8663, USA. Tel.: +1 301 975 4310.

*E-mail address:* [randall.mcdermott@nist.gov](mailto:randall.mcdermott@nist.gov) (R. McDermott).

nonlinear. Transported probability density function (PDF) methods, which have been developed for more than 30 years in a RANS (Reynolds-averaged Navier–Stokes) context, are an elegant means of addressing this problem because the chemical source term conveniently appears in closed form [28]. With improved algorithms and the ever increasing power of digital computers, large-eddy simulation (LES) is becoming a viable alternative to RANS in many areas, including combustion, and new statistical methods are emerging as a result [22,29].

Filtered density function (FDF) methods are the LES analog of PDF methods [29]. Like the PDF transport equation, the FDF transport equation contains an unclosed conditional molecular diffusion term, which must be modeled. There are two aspects of molecular diffusion to be considered: one is the process of *mixing*, which appears as transport in composition space in the PDF and FDF equations; the other is *spatial transport*, which appears as gradient diffusion of the PDF and FDF in physical space. The high dimensionality of the FDF equation necessitates the use of particle methods for its numerical solution. Most of these methods are geared toward high-Reynolds number ( $Re$ ) flows and ignore or treat only approximately the spatial transport aspect of molecular diffusion. This is permissible for RANS. In LES, however, the locally dominant physical processes depend on the filter width and the local viscous length scale. As the filter width becomes small relative to the viscous scale, molecular diffusion needs to be handled accurately. With this motivation in mind, the goals of this paper are: (1) to introduce a model for the conditional molecular diffusion term that allows the FDF formulation – in the limit of vanishing filter width – to yield a direct numerical simulation (DNS) with the appropriate representation of spatial transport by molecular diffusion (including differential diffusion) and (2) to develop a numerical method to solve the modeled equations that (a) is second-order accurate in space and time, (b) achieves detailed conservation, (c) guarantees realizability and boundedness of the scalar field and (d) is unconditionally stable.

Since its introduction by Pope [29], the FDF approach has been developed by several authors. The transport equation for the FDF was first derived by Gao and O'Brien [12]. Colucci et al. [6] developed and tested the scalar FDF method for constant-density chemically-reacting flows. Jaber et al. [16] introduced the filtered mass density function (FMDF) approach for variable-density flows and tested the method in a reacting mixing layer with small density differences (relative to combustion). Gicquel et al. [13] developed the velocity filtered density function (VFDF) approach in which subgrid advection appears in closed form. Sheikhi et al. [35] extended the VFDF approach to include passive scalars and more recently developed the velocity-scalar filtered mass density function (VSFMDF) method for variable-density reacting flows [36]. Various hybrid LES-FMDF methodologies, in which the hydrodynamics is solved by a conventional finite-difference approach and the FMDF is obtained by a Lagrangian particle method, have been developed and successfully applied to modeling a piloted jet flame by Sheikhi et al. [34] and a bluff-body-stabilized flame by Raman et al. [32,33]. Along the same lines, Bisetti and Chen [5] also employ a hybrid strategy, but solve for the FDF with an Eulerian particle method. Lastly, in a recent review article, Givi [14] summarizes the state-of-the-art for FDF methods in turbulent reacting flows.

The most common way of handling molecular diffusion in the approaches listed above is the method introduced by Anand and Pope [1], based largely on the works of Taylor [40], where a set of coupled stochastic differential equations (SDEs) is solved for the particle position and composition: spatial transport is modeled by a Wiener process (random walk) in the position equation and the composition equation contains the mixing model. In light of our first goal, stated above, the problems with this approach are two-fold. First, the Lagrangian particle model just outlined implies a certain Fokker–Planck equation for the FDF. By taking the second moment of this equation one can obtain the evolution equation for the variance of the scalar field. This variance equation contains a spurious production term that does not vanish as the filter width becomes small. Hence, the formulation does not reduce to a DNS in the appropriate limit. Second, spatial transport is achieved by a random walk of the particle in physical space, the magnitude of which is governed by a single molecular diffusion coefficient. Thus, the formulation cannot allow for differential diffusion, which, as is widely acknowledged [3,11,29], can have a first-order effect on combustion processes.

Previous reviews [11,30,38] have listed the properties of an ideal mixing model in the context of RANS modeling. These properties apply strictly to the mixing model (not a mixing *and* transport model) and should be modified slightly in the LES-FDF context. Here we list the desirable properties of an ideal *diffusion* model for FDF computations:

- (i) The model accounts for the spatial transport of the FDF and consequently accounts for the spatial transport of all moments of the FDF.
- (ii) The model captures the decay of the subgrid-scale covariance (see (22) below) and this term vanishes in the DNS limit (further discussed in Section 2.4).
- (iii) Realizability and boundedness principles are obeyed: joint boundedness in the case of equal binary diffusivities and individual boundedness in the case of unequal binary diffusivities.
- (iv) The linearity and independence properties implied by the scalar conservation equation (for the case of equal diffusivities) are obeyed [27].
- (v) The model accounts for differential diffusion at all length scales.
- (vi) The model accounts for the influence of reaction on mixing.
- (vii) The model can be implemented efficiently in a particle method used to solve the FDF equations.

This list is very similar to that given by Pope [30]. Item (i) has been modified because we are considering a combined mixing and transport model: the FDF evolves in physical space due to spatial transport. In Item (ii), we emphasize that the covariance should vanish in the DNS limit (see Section 2.4). Item (vii) is added because given that, as of yet, no one model satisfies all the desirable properties of the ideal model, there are inevitably trade-offs to be made in model selection, and a model's implementation cost and ease of use are often important criteria in this decision.

The method presented in this paper combines a model for spatial transport of the mean with the simple ‘interaction by exchange with the mean’ (IEM) mixing model [9,43], all within the composition equation: there is no random walk based on a molecular diffusivity in the position equation. The model is capable of treating differential diffusion of the mean in a time-accurate way. Spatial transport of the variance, however, is ignored. So, our model partially satisfies Item (i). Our model does not add a spurious production term to the variance equation and so completely satisfies Item (ii). It is to be noted that the model of Anand and Pope [1] behaves in just the opposite way: it correctly models molecular transport of the variance at the expense of introducing the spurious production term. Since molecular transport is minor for highly turbulent flows and variance production is undesirable for laminar flows, our modeling approach is more applicable to LES. Regarding Item (iii), our model satisfies realizability and individual boundedness, with the latter imposing a lower bound on the specified mixing rate. For equal diffusivities, the linearity and independence properties are satisfied (Item (iv)). Item (v) is partially satisfied by our model because differential diffusion is treated for scales equal to or larger than the LES filter width,  $\Delta$ . Since IEM is used as the mixing model, the present method inherits many of IEM's strengths and weaknesses. The degree to which the method mimics IEM depends on the local Reynolds number (based on  $\Delta$ ). As the local Reynolds number becomes large the method approaches pure IEM, and as the local Reynolds number becomes small the method reduces to DNS. That is, with  $\mathcal{L}$  being the characteristic length scale of the flow, the principal advantage of our formulation is that the model results in the correct behavior for  $\Delta/\mathcal{L} \ll 1$ , as molecular transport becomes more important and subfilter fluctuations decrease. The standard IEM model does not account for the effect of reaction on mixing (Item (vi)). It is possible, however, to incorporate a Damköhler-number dependence into the mixing time scale (see, e.g. [19,31]) and that other improvements could be made, such as relaxing toward a conditional mean [20] or using a joint scalar-mixing-frequency formulation [23], which would allow essentially the same mathematical form of the present diffusion model to account for the effect of reaction on mixing. Issues regarding implementation (Item (vii)) are discussed later in the paper. We emphasize that in the DNS limit our method will trivially satisfy *all* the properties of the ideal model. This is a guiding principle in LES model development: a formulation should be equally well suited to perform a DNS.

The remainder of this paper is organized as follows: In Section 2, we present the governing equations for the FDF formulation. We introduce a model for the conditional diffusion term and derive the moment equations for a simplified system that focusses on diffusion. Here we also derive a constraint on the IEM mixing rate that ensures boundedness of the compositions. We then introduce a particle model that *corresponds* to the model FDF system. In Section 3, we develop a numerical method to solve the particle composition equation. For simplicity, the basic algorithm is introduced in the context of a single scalar in 1D. We then show the minor modifications needed to treat multiple scalars in multiple spatial dimensions. Section 4 presents a suite of test problems designed to verify the mixing rate bounds and the spatial and temporal convergence rates.

These cases also serve to illustrate the qualitative properties of the scheme. Finally, conclusions are presented in Section 5.

## 2. Governing equations

This section is organized as follows: In Sections 2.1 and 2.2, we develop the species and enthalpy transport equations which lead to the generalized composition transport equation (12). Readers familiar with this development may wish to skip ahead to this point. In Section 2.3, we develop the LES equations, considering unequal diffusivities, for the filtered composition and subgrid-scale covariance fields. Next, in Section 2.4, we discuss the “DNS limit” of the LES equations. The exact and modeled FDF transport equations are presented in Sections 2.5 and 2.6, respectively. In Section 2.7, we discuss the relationship between the continuous model equations and the particle equations which form the foundation for the numerical method. Lastly, to provide a basis for comparison, in Section 2.8 we briefly describe the random walk transport model.

### 2.1. Species conservation equations

In combustion modeling we often need to consider the transport of several reactant, product, and intermediate species which form a mixture of ideal gases. Here we consider the evolution of  $n_s$  species mass fractions, denoted by  $Y_\alpha(\mathbf{x}, t)$ ;  $0 \leq Y_\alpha \leq 1$ ; for  $\alpha = 1, \dots, n_s$ . In what follows we use Greek subscripts to designate scalar components and Roman subscripts for directional components and implied summation over repeated suffixes applies for both types of indices. However, bracketed suffixes are excluded from the summation convention.

The general species transport equation is

$$\rho \frac{DY_\alpha}{Dt} = - \frac{\partial J_{\alpha,j}}{\partial x_j} + \rho S_\alpha, \quad (1)$$

where  $D/Dt \equiv \partial/\partial t + U_j \partial/\partial x_j$  is the material derivative with  $U_j$  being the local mass-average velocity [41] in the  $x_j$  direction;  $\rho$  is the fluid mass density;  $J_{\alpha,j} \equiv \rho V_{\alpha,j} \equiv \rho(U_{\alpha,j} - U_j)$  is the diffusive mass flux (relative to the mass-average velocity) of species  $\alpha$  in the  $x_j$  direction, with  $\rho U_{\alpha,j}$  being the total flux of  $\alpha$  in the  $x_j$  direction and  $V_{\alpha,j}$  being the component of the “diffusion velocity” for  $\alpha$  in the  $x_j$  direction; and finally  $S_\alpha$  is the reaction source term for species  $\alpha$ .

Note that, by construction, the diffusive mass fluxes sum to zero,  $\sum_{\alpha=1}^{n_s} J_{\alpha,j} = 0$ . Thus, only  $n_s - 1$  of the fluxes are independent. In practice there are two predominant strategies for addressing this issue [26]: (1) either  $n_s - 1$  species transport equations are solved and the composition for species  $n_s$  (usually taken to be the species in highest concentration) is obtained from  $Y_{n_s} = 1 - \sum_{\alpha=1}^{n_s-1} Y_\alpha$ , or (2) a correction is added to the diffusion velocity to enforce the constraint that the diffusion fluxes sum to zero. In the present work, we will adopt the latter strategy. The modifications required of the model and numerical method are discussed below in Sections 2.6.1 and 3.5.5, respectively.

We require a constitutive relation to model the diffusive flux. With  $D_{\alpha\beta}$  being the symmetric matrix of Fickian diffusion coefficients, the general form of Fick’s law is

$$J_{\alpha,j} = -\rho D_{\alpha\beta} \frac{\partial Y_\beta}{\partial x_j}, \quad (2)$$

and accounts for full multi-component mass transport. It should be noted that the Fickian diffusion coefficients are linearly related to the Maxwell–Stefan binary diffusivities [41].

A simplification to the multi-component form, which is often well justified, is to consider “mixture-averaged” diffusivities, such that the diffusive flux of one scalar is decoupled from the gradients of other scalars (equivalently, the Fickian matrix is diagonal). Multi-component effects (e.g. reverse diffusion) are not possible with this approach, but one retains the effects of differential diffusion. The mixture-averaged form of Fick’s law is given by

$$J_{\alpha,j} = -\rho D_{(\alpha)} \frac{\partial Y_\alpha}{\partial x_j}. \quad (3)$$

Recall that there is no summation over the bracketed suffixes in (3). There are many ways of estimating the mixture-averaged diffusivity,  $D_\alpha$ , which is a known function of the thermo-chemical state. The interested reader is referred to [4,37,41].

Although the methods developed here would work equally well for a full multi-component formulation, throughout the remainder of this work we assume the mixture-averaged approach is being applied. The species transport equation may then be written as

$$\rho \frac{DY_\alpha}{Dt} = \frac{\partial}{\partial x_j} \left( \rho D_{(\alpha)} \frac{\partial Y_\alpha}{\partial x_j} \right) + \rho S_\alpha. \tag{4}$$

### 2.2. The enthalpy equation

With some minor simplifications appropriate for low-Mach combustion, the enthalpy transport equation can be written in the same form as (4). Within this subsection we will show summation over species (Greek suffixes explicitly). Let  $h_\alpha(T)$  denote the chemical plus sensible enthalpy of species  $\alpha$  at temperature,  $T$ ,

$$h_\alpha(T) = \Delta h_\alpha^0 + \int_{T_0}^T C_{p,\alpha}(T') dT', \tag{5}$$

where  $\Delta h_\alpha^0$  is the enthalpy of formation of species  $\alpha$  at the reference temperature,  $T_0$ , and  $C_{p,\alpha} \equiv \partial h_\alpha / \partial T$  is the specific heat of species  $\alpha$ . The enthalpy of the mixture is then given by

$$h = \sum_{\alpha=1}^{n_s} Y_\alpha h_\alpha. \tag{6}$$

Without simplifications, the enthalpy transport equation is [26]

$$\rho \frac{Dh}{Dt} = \frac{Dp}{Dt} + \sum_{\alpha=1}^{n_s} F_{\alpha,j} J_{\alpha,j} + \tau_{ij} \mathcal{S}_{ij} + \dot{Q} - \frac{\partial q_j}{\partial x_j} - \frac{\partial}{\partial x_j} \left( \sum_{\alpha=1}^{n_s} h_\alpha J_{\alpha,j} \right), \tag{7}$$

where  $p$  is pressure,  $F_{\alpha,j}$  is a (potentially preferential) body force (e.g. in the presence of a magnetic field ions of different charges will feel “preferential” body forces, whereas gravity always generates a nonpreferential body force),  $\tau_{ij}$  is the viscous stress tensor,  $\mathcal{S}_{ij}$  is the strain-rate tensor,  $\dot{Q}$  is a volumetric heat source (e.g. a spark or an electrical heating coil), and  $q_j$  is the heat flux vector (conduction plus radiation). For low-Mach-number flows we may neglect spatial pressure fluctuations; hence,  $p = p_0(t)$ . For open systems (such as jet flames) the reference pressure,  $p_0(t)$ , is constant. Thus, the term  $Dp/Dt$  may be neglected. Further, we take body forces to be nonpreferential (i.e.  $F_{\alpha,j} = F_j$ ), the neglect of viscous heating is justified for low-Mach-number flows (i.e. we set  $\tau_{ij} \mathcal{S}_{ij} = 0$ ), and we do not consider volumetric heat sources (i.e.  $\dot{Q} = 0$ ). Hence, under these conditions, the first four terms on the right-hand-side (RHS) of (7) can be neglected. Additionally, we do not consider radiative heat transfer in the heat flux vector. It should be noted that all the effects which are neglected here can be included in the source term developed below.

The thermal diffusivity of the mixture is defined as

$$D_{th} \equiv \frac{k}{\rho C_p}, \tag{8}$$

where  $k$  is the thermal conductivity of the mixture and  $C_p = \sum_{\alpha=1}^{n_s} Y_\alpha C_{p,\alpha}$  is the mixture specific heat. We define the component-specific Lewis number by

$$Le_\alpha \equiv \frac{D_{th}}{D_\alpha} = \frac{k}{\rho C_p D_\alpha}. \tag{9}$$

Adopting Fourier’s law for the conductive heat flux and Fick’s law with mixture-averaged diffusivities for the diffusive mass flux, and defining the deviation of the mass diffusivity from the thermal diffusivity as  $D'_\alpha \equiv D_\alpha - D_{th}$ , we may write the enthalpy transport equation as

$$\rho \frac{Dh}{Dt} = \frac{\partial}{\partial x_j} \left( \rho D_{th} \frac{\partial h}{\partial x_j} \right) + \rho S_h, \quad (10)$$

where

$$S_h \equiv \frac{1}{\rho} \frac{\partial}{\partial x_j} \left( \left[ 1 - \sum_{\alpha=1}^{n_s} \frac{Y_\alpha C_{p,\alpha}}{C_p} L e_\alpha^{-1} \right] k \frac{\partial T}{\partial x_j} \right) + \frac{1}{\rho} \frac{\partial}{\partial x_j} \left( \rho \sum_{\alpha=1}^{n_s} D'_\alpha \frac{\partial Y_\alpha h_\alpha}{\partial x_j} \right). \quad (11)$$

This is the extension of the Shvab–Zeldovich form of the energy equation [42] to unequal diffusivities. Notice that (10) is in a form identical to (4), and that  $S_h$  vanishes for unity Lewis numbers (i.e.  $Le_\alpha = 1$ ,  $D'_\alpha = 0$  for all  $\alpha$ ). In the general case, the enthalpy source is small since component Lewis numbers vary near unity [26] and the diffusivity deviations,  $D'_\alpha$ , vary near zero.

We may now consider the general scalar transport equation

$$\rho \frac{D\phi_\alpha}{Dt} = \frac{\partial}{\partial x_j} \left( \rho D_{(\alpha)} \frac{\partial \phi_\alpha}{\partial x_j} \right) + \rho S_\alpha, \quad (12)$$

for the  $n_\phi = n_s + 1$  scalars  $\phi_\alpha = \{Y_1, Y_2, \dots, Y_{n_s}, h\}$ . We will refer to  $\phi$  as the “composition” vector. Note that the mixture-averaged diffusivities are functions of the full thermo-chemical composition,  $D_\alpha = D_\alpha(\phi)$ , and that  $D_{n_\phi} = D_{th}$ .

### 2.3. LES equations

In LES the “large” and “small” scales are formally defined through a spatial filtering operation. The large scales are simulated explicitly and the effects of the small scales must be modeled. We define a filtered field by the convolution of an instantaneous field (e.g.  $\phi(\mathbf{x}, t)$ ) with a filter kernel,  $G(\mathbf{r}; \Delta)$ , of characteristic width  $\Delta$  (for brevity we will henceforth omit  $\Delta$  from the argument list), which we take to be uniform and constant, positive ( $G(\mathbf{r}) \geq 0$ ), symmetric ( $G(\mathbf{r}) = G(-\mathbf{r})$ ) and normalized ( $\int G(\mathbf{r}) d\mathbf{r} = 1$ ). The filtered field of an arbitrary scalar  $\phi$  is then defined as

$$\langle \phi(\mathbf{x}, t) \rangle_\ell \equiv \int G(\mathbf{x} - \mathbf{x}') \phi(\mathbf{x}', t) d\mathbf{x}'. \quad (13)$$

It is also useful to define a mass-weighted filtered field (the “Favre-filtered” field),

$$\langle \phi(\mathbf{x}, t) \rangle_L \equiv \frac{\langle \rho(\mathbf{x}, t) \phi(\mathbf{x}, t) \rangle_\ell}{\langle \rho(\mathbf{x}, t) \rangle_\ell}. \quad (14)$$

A word on notation: the subscript “ $L$ ” was introduced by Colucci et al. [6] to indicate that filtered means were being taken over a given length scale,  $L$ . The same subscript was then adopted by Jaberi et al. [16], who used it to distinguish between the two different filters, (13) and (14), and the filtered means were labeled with subscripts  $\ell$  and  $L$ , respectively. Since Jaberi et al. the notation has become somewhat standard for FDF approaches and so we retain it here to avoid confusion with previous works. However, we still explicitly represent the LES filter width by  $\Delta$ .

Applying (13) and (14) to (12), and using continuity, we obtain the LES scalar transport equation,

$$\frac{\partial \langle \langle \rho \rangle_\ell \langle \phi_\alpha \rangle_L \rangle}{\partial t} + \frac{\partial \langle \langle \rho \rangle_\ell \langle \phi_\alpha \rangle_L \langle U_j \rangle_L \rangle}{\partial x_j} = \frac{\partial}{\partial x_j} \left( \left\langle \left\langle \rho D_{(\alpha)} \frac{\partial \phi_\alpha}{\partial x_j} \right\rangle_\ell \right\rangle \right) + \langle \rho \rangle_\ell \langle S_\alpha \rangle_L - \frac{\partial J_{\alpha,j}^{\text{sgs}}}{\partial x_j}, \quad (15)$$

where

$$J_{\alpha,j}^{\text{sgs}} \equiv \langle \rho \rangle_\ell [ \langle \phi_\alpha U_j \rangle_L - \langle \phi_\alpha \rangle_L \langle U_j \rangle_L ] \quad (16)$$

defines the “subgrid” advective flux.

In LES of reacting flows the focus of most research is to address the closure problems associated with the subgrid-scale (SGS) flux,  $J_{\alpha,j}^{\text{sgs}}$ , and the Favre-filtered source term,  $\langle S_\alpha \rangle_L$  (generally a nonlinear function of all instantaneous compositions). In common LES approaches these terms represent the greatest modeling challenge and are of critical importance in most turbulent reacting flows.

In FDF methods, however, the Favre-filtered *chemical* source term very conveniently appears in closed form (note, however, that the Favre-filtered enthalpy source is *not* closed and will require modeling). Also, it is possible to formulate LES such that the nonlinear advective term is closed, as in the VFDF approach of Gicquel et al. [13]. In these approaches the treatment of the diffusion term is an issue of paramount importance and the modeling of this term is our primary concern here.

The filtered diffusive flux is approximated by

$$\left\langle \rho D_{(\alpha)} \frac{\partial \phi_\alpha}{\partial x_j} \right\rangle_\ell \approx \langle \rho \rangle_\ell \langle D_{(\alpha)} \rangle_L \frac{\partial \langle \phi_\alpha \rangle_L}{\partial x_j}. \tag{17}$$

Eq. (17) is introduced in the interest of developing an LES formulation that reduces to a DNS in the limit  $\Delta/\mathcal{L} \rightarrow 0$ . It is important to recognize that the approximation in (17) does not follow from directly applying (13) and/or (14) to the instantaneous flux term. There is no standard decomposition of the filtered diffusive flux, but our choice (17) is consistent with the treatment of viscous and thermal molecular transport in the compressible formulation of Pino Martín et al. [21]. Note that  $\langle D_{\alpha}(\mathbf{x}, t) \rangle_L$  requires a closure and would either be set to zero or taken to be  $\langle D_{\alpha}(\mathbf{x}, t) \rangle_L \approx D_{\alpha}(\langle \phi[\mathbf{x}, t] \rangle_L)$  in conventional LES formulations [24–26]. In FDF methods the filtered diffusivity, like the chemical source term, is in closed form. With (17), our filtered scalar transport equation can be written as

$$\frac{\partial \langle \rho \rangle_\ell \langle \phi_\alpha \rangle_L}{\partial t} + \frac{\partial \langle \rho \rangle_\ell \langle \phi_\alpha \rangle_L \langle U_j \rangle_L}{\partial x_j} = \frac{\partial}{\partial x_j} \left( \langle \rho \rangle_\ell \langle D_{(\alpha)} \rangle_L \frac{\partial \langle \phi_\alpha \rangle_L}{\partial x_j} \right) + \langle \rho \rangle_\ell \langle S_\alpha \rangle_L - \frac{\partial J_{\alpha,j}^{\text{sgs}}}{\partial x_j}. \tag{18}$$

The focus of this work is to develop an improved treatment of the conditional diffusion term for FDF methods. Therefore, we do not consider advection or source term production. In the test cases to be presented we will omit these terms (i.e. we set  $U_j = 0$  and  $S_\alpha = 0$  for all  $\mathbf{x}$  and  $t$ ). Our filtered scalar transport equation then reduces to

$$\langle \rho \rangle_\ell \frac{\partial \langle \phi_\alpha \rangle_L}{\partial t} = \frac{\partial}{\partial x_j} \left( \langle \rho \rangle_\ell \langle D_{(\alpha)} \rangle_L \frac{\partial \langle \phi_\alpha \rangle_L}{\partial x_j} \right). \tag{19}$$

We are also interested in the behavior of the Favre-“SGS covariance”. Here we denote the SGS covariance of the scalars  $\phi_\alpha$  and  $\phi_\beta$  by  $Z_{\alpha\beta}^{\text{sgs}} \equiv \langle \phi_\alpha \phi_\beta \rangle_L - \langle \phi_\alpha \rangle_L \langle \phi_\beta \rangle_L$ . Making the same approximations used to obtain (17), the transport equation for  $Z_{\alpha\beta}^{\text{sgs}}$  deduced from (12) is

$$\frac{\partial \left( \langle \rho \rangle_\ell Z_{\alpha\beta}^{\text{sgs}} \right)}{\partial t} + \frac{\partial \left( \langle \rho \rangle_\ell Z_{\alpha\beta}^{\text{sgs}} \langle U_j \rangle_L \right)}{\partial x_j} = \mathcal{D}_{\alpha\beta} + \tilde{\chi}_{\alpha\beta} + \mathcal{R}_{\alpha\beta} + \mathcal{P}_{\alpha\beta} + \mathcal{T}_{\alpha\beta}, \tag{20}$$

where the terms on the RHS are, respectively, molecular transport, filter-scale dissipation or production due to alignment of scalar gradients, production due to reaction, turbulent production, and turbulent transport:

$$\mathcal{D}_{\alpha\beta} \equiv \frac{\partial}{\partial x_j} \left( \langle \rho \rangle_\ell \langle D_{(\alpha)} \rangle_L \left[ \left\langle \phi_\beta \frac{\partial \phi_\alpha}{\partial x_j} \right\rangle_L - \langle \phi_\beta \rangle_L \frac{\partial \langle \phi_\alpha \rangle_L}{\partial x_j} \right] \right) + \frac{\partial}{\partial x_j} \left( \langle \rho \rangle_\ell \langle D_{(\beta)} \rangle_L \left[ \left\langle \phi_\alpha \frac{\partial \phi_\beta}{\partial x_j} \right\rangle_L - \langle \phi_\alpha \rangle_L \frac{\partial \langle \phi_\beta \rangle_L}{\partial x_j} \right] \right), \tag{21}$$

$$\tilde{\chi}_{\alpha\beta} \equiv -\langle \rho \rangle_\ell \left[ \langle D_{(\alpha)} \rangle_L + \langle D_{(\beta)} \rangle_L \right] \left( \left\langle \frac{\partial \phi_\alpha}{\partial x_j} \frac{\partial \phi_\beta}{\partial x_j} \right\rangle_L - \frac{\partial \langle \phi_\alpha \rangle_L}{\partial x_j} \frac{\partial \langle \phi_\beta \rangle_L}{\partial x_j} \right), \tag{22}$$

$$\mathcal{R}_{\alpha\beta} \equiv \langle \rho \rangle_\ell \left[ \langle \phi_\alpha S_\beta \rangle_L - \langle \phi_\alpha \rangle_L \langle S_\beta \rangle_L + \langle \phi_\beta S_\alpha \rangle_L - \langle \phi_\beta \rangle_L \langle S_\alpha \rangle_L \right], \tag{23}$$

$$\mathcal{P}_{\alpha\beta} \equiv - \left[ J_{\alpha,j}^{\text{sgs}} \frac{\partial \langle \phi_\beta \rangle_L}{\partial x_j} + J_{\beta,j}^{\text{sgs}} \frac{\partial \langle \phi_\alpha \rangle_L}{\partial x_j} \right], \tag{24}$$

$$\mathcal{T}_{\alpha\beta} \equiv - \frac{\partial}{\partial x_j} \left( \langle \rho \rangle_\ell \left[ \langle \phi_\alpha \phi_\beta U_j \rangle_L - \langle \phi_\alpha \rangle_L \langle \phi_\beta \rangle_L \langle U_j \rangle_L \right] \right) + \frac{\partial}{\partial x_j} \left( \langle \rho \rangle_\ell \left[ \langle \phi_\alpha \rangle_L J_{\beta,j}^{\text{sgs}} + \langle \phi_\beta \rangle_L J_{\alpha,j}^{\text{sgs}} + \langle U_j \rangle_L Z_{\alpha\beta}^{\text{sgs}} \right] \right) \tag{25}$$

(similar expressions, which do not account for differential diffusion, can be found in [36]).

Since we are not addressing issues related to turbulent advection or mean source term production, for simplicity we again take the velocity and source term to be zero. Eq. (20) then simplifies to

$$\langle \rho \rangle_\ell \frac{\partial Z_{\alpha\beta}^{\text{SGS}}}{\partial t} = \mathcal{D}_{\alpha\beta} + \tilde{\chi}_{\alpha\beta}. \quad (26)$$

#### 2.4. The DNS limit

The LES solution depends on the artificial parameter  $\Delta$ , the filter width. With  $\mathcal{L}$  representing the characteristic length scale of the flow, it is important to consider the nature of the LES solution in the limit  $\Delta/\mathcal{L} \rightarrow 0$ , which we refer to as the ‘‘DNS limit.’’ It is so called because in this limit the LES solution tends toward the solution of the governing equations.

Not all LES *model* formulations respect this limit. In fact, as we have mentioned and will discuss in more detail later, the most common approach for treating diffusion in FDF methods results in a formulation which is unsuitable for performing DNS.

The key mathematical implication of the limit is that spatial fluctuations are  $\mathcal{O}(\Delta^2)$  for small  $\Delta$  and tend toward zero,

$$\phi''_\alpha \equiv \phi_\alpha - \langle \phi_\alpha \rangle_L \rightarrow 0, \quad (27)$$

as  $(\Delta/\mathcal{L}) \rightarrow 0$ . Similarly, the SGS covariance tends to zero at the same rate,

$$Z_{\alpha\beta}^{\text{SGS}} \equiv \langle \phi_\alpha \phi_\beta \rangle_L - \langle \phi_\alpha \rangle_L \langle \phi_\beta \rangle_L \rightarrow 0, \quad (28)$$

as shown by the seminal work of Leonard [18]. The same holds for velocity fluctuations, velocity-scalar SGS covariances and higher-order SGS correlations. Consequently, the LES equations (e.g. (18)) tend toward the governing transport equations (e.g. (12)) in the DNS limit. Clearly, it is desirable that the LES model formulation exhibits the same limiting behavior.

#### 2.5. The exact FDF transport equation

For our purposes it is sufficient to work in terms of the composition FDF (because we are not addressing issues regarding turbulent advection there is no advantage in using a VFDF). We consider  $n_\phi = n_s + 1$  random scalar fields  $\phi(\mathbf{x}, t)$ , with  $\psi \equiv \{\psi_1, \psi_2, \dots, \psi_{n_\phi}\}$  being sample space variables for each composition. A starting point for the development of the transport equation for the composition FDF is to consider the ‘‘fine-grained joint-PDF’’ of scalar compositions,  $f'(\psi; \mathbf{x}, t)$ , defined as a product of Dirac delta functions,

$$f'(\psi; \mathbf{x}, t) \equiv \prod_{\alpha=1}^{n_\phi} \delta(\phi_\alpha[\mathbf{x}, t] - \psi_\alpha) \equiv \delta(\phi[\mathbf{x}, t] - \psi). \quad (29)$$

Following Jaberi et al. [16], we then define the joint scalar composition ‘‘filtered mass density function’’ (FMDF) by

$$F_L(\psi; \mathbf{x}, t) \equiv \int G(\mathbf{x} - \mathbf{x}') \rho(\mathbf{x}', t) f'(\psi; \mathbf{x}', t) d\mathbf{x}'. \quad (30)$$

For an arbitrary random function,  $Q(\mathbf{x}, t)$ , the conditionally filtered field,  $\langle Q|\psi \rangle_L \equiv \langle Q(\mathbf{x}, t) | \phi(\mathbf{x}, t) = \psi \rangle_L$ , is defined by

$$\langle Q|\psi \rangle_L \equiv \frac{\int G(\mathbf{x} - \mathbf{x}') \rho(\mathbf{x}', t) Q(\mathbf{x}', t) \delta(\phi[\mathbf{x}', t] - \psi) d\mathbf{x}'}{F_L(\psi; \mathbf{x}, t)}. \quad (31)$$

From the properties of the Dirac delta function we obtain the following mathematical relationship for the fine-grained PDF [30],

$$\frac{\partial f'}{\partial t} + U_j \frac{\partial f'}{\partial x_j} = - \frac{\partial}{\partial \psi_\alpha} \left[ f' \frac{D\phi_\alpha}{Dt} \right]. \quad (32)$$



Utilizing (31) we can multiply (29) by  $\rho$  and  $G$  and integrate over physical space to obtain an analogous relationship for the FMDF,

$$\frac{\partial F_L}{\partial t} + \frac{\partial}{\partial x_j} [F_L \langle U_j | \psi \rangle_L] = - \frac{\partial}{\partial \psi_\alpha} \left[ F_L \left\langle \frac{D\phi_\alpha}{Dt} \middle| \psi \right\rangle_L \right]. \tag{33}$$

Eq. (33) follows from the definitions (30) and (31), and the mathematical properties of the Dirac delta function. The physics is introduced by substitution of (12) into (33), which yields

$$\frac{\partial F_L}{\partial t} + \frac{\partial}{\partial x_j} [F_L \langle U_j | \psi \rangle_L] = - \frac{\partial}{\partial \psi_\alpha} \left[ F_L \left\langle \frac{1}{\rho} \frac{\partial}{\partial x_j} \left( \rho D_{(x)} \frac{\partial \phi_\alpha}{\partial x_j} \right) \middle| \psi \right\rangle_L \right] - \frac{\partial}{\partial \psi_\alpha} [F_L S_\alpha]. \tag{34}$$

When the mixture-averaged form of the diffusive flux is employed (34) is the exact transport equation to be solved in FMDF methods for turbulent reacting flows. Note that the chemical source term (i.e.  $S_\alpha$  for  $\alpha = 1, \dots, n_s$ ) appears in closed form since, due to (31),  $\langle S_\alpha(\phi[\mathbf{x}, t]) | \phi(\mathbf{x}, t) = \psi \rangle_L = S_\alpha(\psi)$ . However, the enthalpy source, the conditional advection and the conditional diffusion terms are unclosed and require modeling.

A simple treatment of the enthalpy source, which for the first moment amounts to a similar level of approximation as made in (17) and becomes exact in the DNS limit, is (with summation over  $\alpha$  shown explicitly)

$$S_h \approx \frac{1}{\langle \rho \rangle_\ell} \frac{\partial}{\partial x_j} \left( \left\langle \left[ 1 - \sum_{\alpha=1}^{n_s} \frac{Y_\alpha C_{p,\alpha}}{C_p} L e_\alpha^{-1} \right] k \right\rangle_L \frac{\partial \langle T \rangle_L}{\partial x_j} \right) + \frac{1}{\langle \rho \rangle_\ell} \frac{\partial}{\partial x_j} \left( \langle \rho \rangle_\ell \sum_{\alpha=1}^{n_s} \langle D'_\alpha \rangle_L \frac{\partial \langle Y_\alpha h_\alpha \rangle_L}{\partial x_j} \right). \tag{35}$$

In a realistic turbulent combustion simulation the treatment of the unclosed advection term is critical. The reader is referred to [16,33,35] for detailed discussions. In this paper we are concerned with handling the unclosed conditional diffusion term, and as mentioned, because of this we will omit the advection term and the chemical and enthalpy source terms. Our exact FMDF transport equation then reduces to

$$\frac{\partial F_L}{\partial t} = - \frac{\partial}{\partial \psi_\alpha} \left[ F_L \left\langle \frac{1}{\rho} \frac{\partial}{\partial x_j} \left( \rho D_{(x)} \frac{\partial \phi_\alpha}{\partial x_j} \right) \middle| \psi \right\rangle_L \right]. \tag{36}$$

By taking moments of the FMDF equation it is possible to obtain the same transport equations for the Favre-filtered scalar field and Favre-SGS covariance as were derived by filtering the scalar transport equation. This fact is illustrated below for our simplified system.

By design, the zeroth moment of the FMDF is the filtered density,

$$\int F_L(\psi; \mathbf{x}, t) \, d\psi = \langle \rho \rangle_\ell, \tag{37}$$

and the first moment of the FMDF is

$$\int \psi_\alpha F_L(\psi; \mathbf{x}, t) \, d\psi = \langle \rho \phi_\alpha \rangle_\ell \equiv \langle \rho \rangle_\ell \langle \phi_\alpha \rangle_L. \tag{38}$$

Thus, multiplying (36) by  $\psi_\alpha$  and integrating over all scalar space yields (19), confirming that the first moment of the FMDF equation is equivalent to the transport equation obtained from filtering (12), after introducing the approximation (17).

The second-order moments of the FMDF are

$$\int \psi_\alpha \psi_\beta F_L(\psi; \mathbf{x}, t) \, d\psi = \langle \rho \rangle_\ell \langle \phi_\alpha \phi_\beta \rangle_L. \tag{39}$$

Using the same procedure outlined above, we multiply (36) by  $\psi_\alpha \psi_\beta$  and integrate over the multi-dimensional scalar space and use continuity to obtain

$$\begin{aligned} \langle \rho \rangle_\ell \frac{\partial \langle \phi_\alpha \phi_\beta \rangle_L}{\partial t} &= \frac{\partial}{\partial x_j} \left( \langle \rho \rangle_\ell \langle D_{(\beta)} \rangle_L \left\langle \phi_\alpha \frac{\partial \phi_\beta}{\partial x_j} \right\rangle_L \right) + \frac{\partial}{\partial x_j} \left( \langle \rho \rangle_\ell \langle D_{(\alpha)} \rangle_L \left\langle \phi_\beta \frac{\partial \phi_\alpha}{\partial x_j} \right\rangle_L \right) - \langle \rho \rangle_\ell [\langle D_{(\alpha)} \rangle_L \\ &+ \langle D_{(\beta)} \rangle_L] \left\langle \frac{\partial \phi_\alpha}{\partial x_j} \frac{\partial \phi_\beta}{\partial x_j} \right\rangle_L, \end{aligned} \quad (40)$$

where again we have made approximations similar to (17),

$$\left\langle \rho D_{(\alpha)} \phi_\beta \frac{\partial \phi_\alpha}{\partial x_j} \right\rangle_\ell \approx \langle \rho \rangle_\ell \langle D_{(\alpha)} \rangle_L \left\langle \phi_\beta \frac{\partial \phi_\alpha}{\partial x_j} \right\rangle_L, \quad (41)$$

and

$$\left\langle \rho D_{(\alpha)} \frac{\partial \phi_\alpha}{\partial x_j} \frac{\partial \phi_\beta}{\partial x_j} \right\rangle_\ell \approx \langle \rho \rangle_\ell \langle D_{(\alpha)} \rangle_L \left\langle \frac{\partial \phi_\alpha}{\partial x_j} \frac{\partial \phi_\beta}{\partial x_j} \right\rangle_L. \quad (42)$$

Note that the Favre-filtered diffusivity may be obtained from

$$\langle D_\alpha(\mathbf{x}, t) \rangle_L = \frac{1}{\langle \rho \rangle_\ell} \int D_\alpha(\boldsymbol{\psi}) F_L(\boldsymbol{\psi}; \mathbf{x}, t) \, d\boldsymbol{\psi}. \quad (43)$$

Next, multiplying (19) by  $\langle \phi_\beta \rangle_L$ , transposing indices, and adding the two results gives

$$\begin{aligned} \langle \rho \rangle_\ell \frac{\partial (\langle \phi_\alpha \rangle_L \langle \phi_\beta \rangle_L)}{\partial t} &= \frac{\partial}{\partial x_j} \left( \langle \rho \rangle_\ell \langle D_{(\alpha)} \rangle_L \langle \phi_\beta \rangle_L \frac{\partial \langle \phi_\alpha \rangle_L}{\partial x_j} \right) + \frac{\partial}{\partial x_j} \left( \langle \rho \rangle_\ell \langle D_{(\beta)} \rangle_L \langle \phi_\alpha \rangle_L \frac{\partial \langle \phi_\beta \rangle_L}{\partial x_j} \right) - \langle \rho \rangle_\ell [\langle D_{(\alpha)} \rangle_L \\ &+ \langle D_{(\beta)} \rangle_L] \frac{\partial \langle \phi_\alpha \rangle_L}{\partial x_j} \frac{\partial \langle \phi_\beta \rangle_L}{\partial x_j}. \end{aligned} \quad (44)$$

By subtracting (44) from (40) we obtain (26), confirming that the SGS covariance can be obtained through the second-order moment of the FMDF.

## 2.6. The modeled FDF transport equation

With  $U_j$  and  $S_\alpha$  taken to be zero, the exact FMDF transport equation is (36). This equation is unclosed since, given the distribution  $F_L$ , we cannot evaluate the scalar gradients in the diffusion term. Here we introduce a closure for the conditional diffusion term that combines a model for spatial transport of the mean with the IEM mixing model. Let  $\omega(\mathbf{x}, t)$  represent the IEM turbulent mixing frequency, which is a specified function of space and time (i.e. it is supplied by a separate part of the LES formulation). Our model FMDF equation (for the simplified system) is

$$\frac{\partial F_L}{\partial t} = - \frac{\partial}{\partial \psi_\alpha} \left( F_L \left[ \frac{1}{\langle \rho \rangle_\ell} \frac{\partial}{\partial x_j} \left( \langle \rho \rangle_\ell \langle D_{(\alpha)} \rangle_L \frac{\partial \langle \phi_\alpha \rangle_L}{\partial x_j} \right) + \omega (\langle \phi_\alpha \rangle_L - \psi_\alpha) \right] \right). \quad (45)$$

Eq. (45) is closed because  $\psi_\alpha$  is an independent variable and  $\langle \rho \rangle_\ell$ ,  $\langle \phi_\alpha \rangle_L$ , and  $\langle D_\alpha \rangle_L$  can be obtained from  $F_L$ .

Taking the first moment of (45) yields the modeled equation for the Favre-filtered scalar field,

$$\langle \rho \rangle_\ell \frac{\partial \langle \phi_\alpha \rangle_L}{\partial t} = \frac{\partial}{\partial x_j} \left( \langle \rho \rangle_\ell \langle D_{(\alpha)} \rangle_L \frac{\partial \langle \phi_\alpha \rangle_L}{\partial x_j} \right), \quad (46)$$

which is identical to (19). To obtain the the model equation for the SGS covariance, as before, we first take the second-order moment of the model FMDF,

$$\begin{aligned} \langle \rho \rangle_\ell \frac{\partial \langle \phi_\alpha \phi_\beta \rangle_L}{\partial t} &= \langle \phi_\beta \rangle_L \frac{\partial}{\partial x_j} \left( \langle \rho \rangle_\ell \langle D_{(\alpha)} \rangle_L \frac{\partial \langle \phi_\alpha \rangle_L}{\partial x_j} \right) + \langle \rho \rangle_\ell \omega [\langle \phi_\alpha \rangle_L \langle \phi_\beta \rangle_L - \langle \phi_\alpha \phi_\beta \rangle_L] \\ &+ \langle \phi_\alpha \rangle_L \frac{\partial}{\partial x_j} \left( \langle \rho \rangle_\ell \langle D_{(\beta)} \rangle_L \frac{\partial \langle \phi_\beta \rangle_L}{\partial x_j} \right) + \langle \rho \rangle_\ell \omega [\langle \phi_\beta \rangle_L \langle \phi_\alpha \rangle_L - \langle \phi_\beta \phi_\alpha \rangle_L]. \end{aligned} \quad (47)$$

Next, we multiply (46) by  $\langle \phi_\beta \rangle_L$ , transpose indices, and add the results, to obtain

$$\langle \rho \rangle_\ell \frac{\partial (\langle \phi_\alpha \rangle_L \langle \phi_\beta \rangle_L)}{\partial t} = \langle \phi_\beta \rangle_L \frac{\partial}{\partial x_j} \left( \langle \rho \rangle_\ell \langle D_{(\alpha)} \rangle_L \frac{\partial \langle \phi_\alpha \rangle_L}{\partial x_j} \right) + \langle \phi_\alpha \rangle_L \frac{\partial}{\partial x_j} \left( \langle \rho \rangle_\ell \langle D_{(\beta)} \rangle_L \frac{\partial \langle \phi_\beta \rangle_L}{\partial x_j} \right). \tag{48}$$

Thus, subtracting (48) from (47) yields the model transport equation for the SGS covariance (in the simplified system),

$$\langle \rho \rangle_\ell \frac{\partial Z_{\alpha\beta}^{\text{sgs}}}{\partial t} = -2\omega \langle \rho \rangle_\ell Z_{\alpha\beta}^{\text{sgs}}. \tag{49}$$

The RHS of (49) is a model for  $\tilde{\chi}_{\alpha\beta}$  in (26). There is no equivalent of  $\mathcal{D}_{\alpha\beta}$  in (49), and hence the model does not account for spatial transport of the SGS scalar covariance.

### 2.6.1. Realizability and boundedness constraints

The purpose of this section is to distinguish between *realizability*, *joint boundedness* and *individual boundedness*, and to establish which constraints are relevant to our model system. We show that boundedness of the scalar field is guaranteed by placing a physically motivated lower limit on the mixing rate.

The composition field is *realizable* if  $\phi_\alpha(\mathbf{x}, t) \geq 0$  for  $\alpha = \{1, \dots, n_s\}$  and  $\sum_{\alpha=1}^{n_s} \phi_\alpha(\mathbf{x}, t) = 1$  for all  $\mathbf{x}$  and  $t$ . The same restrictions apply to the filtered field. By summing (46) over species we can see that a necessary condition for an initially realizable field to remain realizable is

$$\langle \rho \rangle_\ell \frac{\partial \sum_{\alpha=1}^{n_s} \langle \phi_\alpha \rangle_L}{\partial t} = \frac{\partial}{\partial x_j} \left( \langle \rho \rangle_\ell \sum_{\alpha=1}^{n_s} \langle D_{(\alpha)} \rangle_L \frac{\partial \langle \phi_\alpha \rangle_L}{\partial x_j} \right) = 0. \tag{50}$$

One can correct the “diffusion velocity”,  $\langle D_{(\alpha)} \rangle_L \partial \langle \phi_\alpha \rangle_L / \partial x_j$ , so that (50) is satisfied [26]. The FMDF diffusion model is then written as

$$\frac{\partial F_L}{\partial t} = - \frac{\partial}{\partial \psi_\alpha} \left( F_L \left[ \frac{1}{\langle \rho \rangle_\ell} \frac{\partial}{\partial x_j} \left( \langle \rho \rangle_\ell V_{\alpha,j}^L \right) + \omega (\langle \phi_\alpha \rangle_L - \psi_\alpha) \right] \right), \tag{51}$$

where the corrected diffusion velocity is

$$V_{\alpha,j}^L \equiv \langle D_{(\alpha)} \rangle_L \frac{\partial \langle \phi_\alpha \rangle_L}{\partial x_j} - \frac{1}{n_s} \sum_{\beta=1}^{n_s} \langle D_{(\beta)} \rangle_L \frac{\partial \langle \phi_\beta \rangle_L}{\partial x_j}. \tag{52}$$

The resulting moment equations derived from (51) satisfy the realizability constraints. In what follows we continue to work with the uncorrected form of the model (45) and revisit the realizability constraint again in designing the numerical method (see Section 3.5.5).

We now turn to the topic of boundedness. In the composition space, let  $\mathcal{C}(t)$  denote the convex hull of all compositions  $\phi_\alpha(\mathbf{x}, t)$  at time  $t$ . For conserved passive scalars with equal diffusivities, a property of the transport equation is that the solution at forward times,  $t_2 > t_1$ , is contained within the convex hull of the solution at time  $t_1$ . Thus, *joint boundedness* dictates that the convex hull cannot expand with time, i.e.  $\mathcal{C}(t_2) \in \mathcal{C}(t_1)$ . Models used for passive scalar transport with equal diffusivities should mimic this property of preserving joint boundedness.

For the case of unequal diffusivities or multi-component mass transport, however, the joint boundedness constraint does not hold. In the case of unequal (binary) diffusivities conserved scalars are subject to the weaker, more general constraint of *individual boundedness*: the scalar field should remain within its own bounds,  $\min_{\mathbf{x}}(\phi_\alpha[\mathbf{x}, t_1]) \leq \phi_\alpha(\mathbf{x}, t_2) \leq \max_{\mathbf{x}}(\phi_\alpha[\mathbf{x}, t_1])$  for all  $\mathbf{x}$  and  $t_2 > t_1$ . In the case of multi-component transport even individual boundedness is not guaranteed due to the process of “reverse diffusion” [41]. While our method does not guarantee joint boundedness in the case of equal diffusivities, it does ensure individual boundedness for the more general case of unequal (binary) diffusivities.

Preserving individual boundedness requires a constraint on the turbulent mixing frequency, as we now show. Let  $\phi_{\alpha,\min}(t) \equiv \min_{\mathbf{x}}(\phi_\alpha[\mathbf{x}, t])$  and  $\phi_{\alpha,\max}(t) \equiv \max_{\mathbf{x}}(\phi_\alpha[\mathbf{x}, t])$ . For realizability we require  $F_L \geq 0$  for all  $\psi$  and for individual boundedness we require  $F_L(\psi; \mathbf{x}, t) = 0$  for  $\psi_\alpha < \phi_{\alpha,\min}(t)$  and  $\psi_\alpha > \phi_{\alpha,\max}(t)$  for all  $\mathbf{x}$ . Note that we may rewrite (45) as

$$\frac{\partial F_L}{\partial t} = - \left[ \frac{\partial \langle \phi_x \rangle_L}{\partial t} + \omega (\langle \phi_x \rangle_L - \psi_x) \right] \frac{\partial F_L}{\partial \psi_x} + \omega F_L, \quad (53)$$

where

$$\frac{\partial \langle \phi_x \rangle_L}{\partial t} = \frac{1}{\langle \rho \rangle_\ell} \frac{\partial}{\partial x_j} \left( \langle \rho \rangle_\ell \langle D_{(x)} \rangle_L \frac{\partial \langle \phi_x \rangle_L}{\partial x_j} \right). \quad (54)$$

The bracketed term in (53) is an advecting “velocity” in  $\psi$ -space. One can always envision adding fluid at the scalar bounds with vanishing probability. Therefore, to guarantee individual boundedness we also require

$$\left[ \frac{\partial \langle \phi_x \rangle_L}{\partial t} + \omega (\langle \phi_x \rangle_L - \psi_x) \right]_{\psi_x = \phi_{x,\max}(t)} \leq 0, \quad (55)$$

and

$$\left[ \frac{\partial \langle \phi_x \rangle_L}{\partial t} + \omega (\langle \phi_x \rangle_L - \psi_x) \right]_{\psi_x = \phi_{x,\min}(t)} \geq 0. \quad (56)$$

In other words, the scalar “velocity” on the boundary of the individual (1D) scalar space must be zero or point toward the interior of the bounded interval. Based on (55) and (56), in order for the model (45) to guarantee individual boundedness, we require that the specified value of the mixing rate satisfy

$$\omega(\mathbf{x}, t) \geq \omega_{\min}(\mathbf{x}, t) \equiv \max_x \left( \left[ \frac{\partial \langle \phi_x(\mathbf{x}, t) \rangle_L / \partial t}{\phi_{x,\min}(t) - \langle \phi_x(\mathbf{x}, t) \rangle_L} \right], \left[ \frac{\partial \langle \phi_x(\mathbf{x}, t) \rangle_L / \partial t}{\phi_{x,\max}(t) - \langle \phi_x(\mathbf{x}, t) \rangle_L} \right] \right). \quad (57)$$

The interpretation of this bound is that compositions close to the boundary must relax toward the mean as fast as or faster than the rate at which the mean is moving toward the boundary. There always exists a mixing rate such that this condition holds. Hence, for our diffusion model the constraint (57) simply ensures that the problem is well-posed.

## 2.7. Continuous and particle systems

As discussed by Pope [30], it is important to distinguish between the turbulent flow model and the particle method used to solve the model equations. The continuum fluid model (e.g. (45)) governs what we will call the *continuous system* and the particle model (to be determined) governs the *particle system*. Our aim is to achieve a *correspondence* between these two systems, as described below.

### 2.7.1. Continuous system

The FMDF transport equation (45) is a deterministic model subject to random initial conditions (i.c.s.) and boundary conditions (b.c.s). For a given set of i.c.s. and b.c.s., the solution of the transport equation uniquely determines one realization of the filtered field. This is the continuous system. Note that the continuous system is the model analog of the exact *fluid system* as discussed in [30].

### 2.7.2. Particle system

Due to the high dimensionality of  $F_L$ , the numerical solution of (45) via a finite-difference method is intractable. Instead, it is typical to employ a Lagrangian particle method [28]. A general particle possesses the properties of mass, position, velocity and composition, denoted  $m^*$ ,  $\mathbf{X}^*(t)$ ,  $\mathbf{U}^*(t)$  and  $\phi^*(t)$ , respectively (superscript indices will be used to distinguish particles and the superscript asterisk denotes a general particle). We wish to represent the FMDF by an ensemble of such particles within the computational domain. These particles together with their properties and evolution equations for their properties comprise the particle system.

For the particle system it is convenient to work in terms of the *mass density function*, denoted  $F_{\phi X}^*(\psi, \mathbf{x}; t)$ . Let  $M$  represent the total mass of fluid in a closed or periodic domain so that  $M$  is constant. This mass is equally distributed among  $N$  particles such that each particle has mass  $m = M/N$ . The initial position of the  $i$ th particle, which is random, is  $\mathbf{X}^{(i)}(t_0)$ . In general, we consider the fluid particle to follow a trajectory

defined by a random velocity field (even if the filtered field is deterministic the fluctuations are not) and so the current particle position,  $\mathbf{X}^{(i)}(t)$ , is also random, as is the current particle composition,  $\phi^{(i)}(t)$ . We first define the discrete mass density function to be

$$F_N^*(\psi, \mathbf{x}; t) \equiv \frac{M}{N} \sum_{i=1}^N \delta(\phi^{(i)}[t] - \psi) \delta(\mathbf{X}^{(i)}[t] - \mathbf{x}). \tag{58}$$

The expectation of  $F_N^*$  is the mass density function (MDF),

$$F_{\phi_X}^*(\psi, \mathbf{x}; t) \equiv \langle F_N^*(\psi, \mathbf{x}; t) \rangle = M \langle \delta(\phi^*[t] - \psi) \delta(\mathbf{X}^*[t] - \mathbf{x}) \rangle = M f_{\phi_X}^*(\psi, \mathbf{x}; t) = M f_X^*(\mathbf{x}; t) f_{\phi|X}^*(\psi; t|\mathbf{x}), \tag{59}$$

where  $f_{\phi_X}^*$  denotes the joint-PDF of particle position and composition,  $f_X^*$  is the marginal PDF of particle position, and  $f_{\phi|X}^*$  is the PDF of particle composition conditional on particle position.

### 2.7.3. Correspondence

As mentioned, our goal is to achieve a correspondence between the continuous and particle systems. This means that we seek a specification of the particle system (i.c.s., b.c.s. and particle property evolution equations) such that  $F_{\phi_X}^*(\psi, \mathbf{x}; t) = F_L(\psi; \mathbf{x}, t)$ , where  $F_L$  evolves by (45) with a given set of i.c.s. and b.c.s.

Note that the following left-right arrow symbol,  $\iff$ , is to be read, ‘‘corresponds to’’. Consider the following correspondence,

$$F_L(\psi; \mathbf{x}, t) \iff F_{\phi_X}^*(\psi, \mathbf{x}; t). \tag{60}$$

Then the zeroth moment of the FMDF, which is the filtered density, corresponds to the zeroth moment of the MDF,

$$\langle \rho \rangle_\ell \iff \int F_{\phi_X}^*(\psi, \mathbf{x}; t) d\psi = M \langle \delta(\mathbf{X}^*[t] - \mathbf{x}) \rangle = M f_X^*(\mathbf{x}; t) \equiv \bar{\rho}. \tag{61}$$

Here we have introduced the short-hand notation that  $\bar{\rho}$  denotes the mean particle mass density.

The first moment of the FMDF corresponds to the first moment of the MDF,

$$\langle \rho \rangle_\ell \langle \phi_\alpha \rangle_L \iff \int \psi_\alpha F_{\phi_X}^*(\psi, \mathbf{x}; t) d\psi = M \langle \phi_\alpha^* \delta(\mathbf{X}^*[t] - \mathbf{x}) \rangle = \bar{\rho} \langle \phi_\alpha^* | \mathbf{x} \rangle, \tag{62}$$

and so evidently the Favre-filtered composition field corresponds to the mean particle composition conditional upon the particle position,

$$\langle \phi_\alpha \rangle_L \iff \langle \phi_\alpha^* | \mathbf{x} \rangle \equiv \tilde{\phi}_\alpha. \tag{63}$$

Notice that here, again for notational convenience, we have denoted the particle conditional mean field with a tilde.

For the second-order moment we have

$$\langle \rho \rangle_\ell \langle \phi_\alpha \phi_\beta \rangle_L \iff \int \psi_\alpha \psi_\beta F_{\phi_X}^*(\psi, \mathbf{x}; t) d\psi = M \langle \phi_\alpha^* \phi_\beta^* \delta(\mathbf{X}^*[t] - \mathbf{x}) \rangle = \bar{\rho} \langle \phi_\alpha^* \phi_\beta^* | \mathbf{x} \rangle, \tag{64}$$

and so the corresponding SGS covariance in the particle system is

$$Z_{\alpha\beta}^{\text{SGS}} \equiv \langle \phi_\alpha \phi_\beta \rangle_L - \langle \phi_\alpha \rangle_L \langle \phi_\beta \rangle_L \iff \langle \phi_\alpha^* \phi_\beta^* | \mathbf{x} \rangle - \langle \phi_\alpha^* | \mathbf{x} \rangle \langle \phi_\beta^* | \mathbf{x} \rangle \equiv \tilde{Z}_{\alpha\beta}. \tag{65}$$

Additionally, the filtered diffusivity in the continuous system corresponds to the particle system diffusivity by

$$\langle D_\alpha \rangle_L \iff \frac{1}{\bar{\rho}} \int D_\alpha(\psi) F_{\phi_X}^*(\psi, \mathbf{x}; t) d\psi = \frac{M}{\bar{\rho}} \langle D_\alpha(\phi^*[t]) \delta(\mathbf{X}^*[t] - \mathbf{x}) \rangle = \langle D_\alpha(\phi^*) | \mathbf{x} \rangle \equiv \tilde{D}_\alpha. \tag{66}$$

Given that at the initial time  $t_0$  we have specified  $F_{\phi_X}^*(\psi, \mathbf{x}; t_0) = F_L(\psi; \mathbf{x}, t_0)$  and that  $F_L$  evolves by (45), the question becomes: How should the particle properties evolve to maintain correspondence? The answer is:

$$\frac{dX_j^*(t)}{dt} = 0, \tag{67}$$

$$\frac{d\phi_\alpha^*(t)}{dt} = \left[ \frac{1}{\bar{\rho}} \frac{\partial}{\partial x_j} \left( \bar{\rho} \tilde{D}_{(\alpha)} \frac{\partial \tilde{\phi}_\alpha}{\partial x_j} \right) \right]_{\mathbf{x}=\mathbf{X}^*(t),t} + \omega(\mathbf{X}^*[t], t) [\tilde{\phi}_\alpha(\mathbf{X}^*[t], t) - \phi_\alpha^*(t)]. \tag{68}$$

Note that the Eulerian fields and gradients thereof are evaluated at the particle position. For later utility we note that (75) may be rewritten to look similar to the IEM model:

$$\frac{d\phi_\alpha^*(t)}{dt} = \omega(\mathbf{X}^*[t], t) [a_\alpha^*(t) - \phi_\alpha^*(t)]. \tag{69}$$

We refer to  $a_\alpha^*(t)$  as the ‘‘particle attractor’’ for species  $\alpha$  and it is defined by

$$a_\alpha^*(t) \equiv \left[ \frac{1}{\omega \bar{\rho}} \frac{\partial}{\partial x_j} \left( \bar{\rho} \tilde{D}_{(\alpha)} \frac{\partial \tilde{\phi}_\alpha}{\partial x_j} \right) \right]_{\mathbf{x}=\mathbf{X}^*(t),t} + \tilde{\phi}_\alpha(\mathbf{X}^*[t], t). \tag{70}$$

Note that a necessary and sufficient condition to *guarantee* individual boundedness of the particle field is that the particle attractor satisfies the same bounds as the composition, i.e.

$$\phi_{\alpha,\min}(t) \leq a_\alpha^*(t) \leq \phi_{\alpha,\max}(t) \quad \text{for all } \mathbf{X}^*(t). \tag{71}$$

Based on (59) and (68) it follows (for a constant mass system) that the particle MDF evolves by

$$\frac{\partial F_{\phi X}^*}{\partial t} = - \frac{\partial}{\partial \psi_\alpha} \left( F_{\phi X}^* \left[ \frac{1}{\bar{\rho}} \frac{\partial}{\partial x_j} \left( \bar{\rho} \tilde{D}_{(\alpha)} \frac{\partial \tilde{\phi}_\alpha}{\partial x_j} \right) + \omega(\tilde{\phi}_\alpha - \psi_\alpha) \right] \right), \tag{72}$$

which corresponds to (45). Thus, a key point to appreciate about FDF methods is this: *Despite the fact that  $F_L$  and  $F_{\phi X}^*$  have quite different physical interpretations, in that the former is defined in terms of a physical space filter and the latter is based on a statistical expectation, a particle system can be designed such that the model FMDF evolution equation and particle MDF evolution equation have the same form and hence, with corresponding i.c.s. and b.c.s., their solutions are identical. A particle method capable of solving (68) yields discrete samples from the MDF, which is statistically equivalent to generating discrete samples from the FMDF.*

It should be appreciated that correspondence is achieved at the level of the FMDF and MDF distributions. It follows that all moment equations obtained from these distributions correspond. For completeness we now show the first and second moment equations obtained from the particle MDF. Multiplying (72) by  $\psi_\alpha$  and integrating over composition space yields

$$\bar{\rho} \frac{\partial \tilde{\phi}_\alpha}{\partial t} = \frac{\partial}{\partial x_j} \left( \bar{\rho} \tilde{D}_{(\alpha)} \frac{\partial \tilde{\phi}_\alpha}{\partial x_j} \right), \tag{73}$$

which corresponds with (46). Following derivations similar to (47) and (48), we find that the evolution of the SGS covariance in the particle system is

$$\bar{\rho} \frac{\partial \tilde{Z}_{\alpha\beta}}{\partial t} = -2\omega \bar{\rho} \tilde{Z}_{\alpha\beta}, \tag{74}$$

in accord with (49).

Note that when employing a corrected diffusion velocity  $F_L$  evolves by (51) and the corresponding particle composition evolution equation is

$$\frac{d\phi_\alpha^*(t)}{dt} = \left[ \frac{1}{\bar{\rho}} \frac{\partial}{\partial x_j} (\bar{\rho} \tilde{V}_{\alpha,j}) \right]_{\mathbf{x}=\mathbf{X}^*(t),t} + \omega(\mathbf{X}^*[t], t) [\tilde{\phi}_\alpha(\mathbf{X}^*[t], t) - \phi_\alpha^*(t)], \tag{75}$$

where the corrected diffusion velocity for the particle system is

$$\tilde{V}_{\alpha,j} \equiv \tilde{D}_{(\alpha)} \frac{\partial \tilde{\phi}_\alpha}{\partial x_j} - \frac{1}{n_s} \sum_{\beta=1}^{n_s} \tilde{D}_{(\beta)} \frac{\partial \tilde{\phi}_\beta}{\partial x_j}. \tag{76}$$

Thus, the particle MDF evolves by

$$\frac{\partial F_{\phi X}^*}{\partial t} = -\frac{\partial}{\partial \psi_\alpha} \left( F_{\phi X}^* \left[ \frac{1}{\bar{\rho}} \frac{\partial}{\partial x_j} (\bar{\rho} \tilde{V}_{\alpha j}) + \omega(\tilde{\phi}_\alpha - \psi_\alpha) \right] \right). \quad (77)$$

### 2.8. The random walk transport model

For comparison we briefly review the conventional formulation for treating molecular diffusion in FDF methods (see, e.g. [16,33]), which uses a random walk model for transport and the IEM model for mixing. The single diffusion coefficient may be taken as a function of the thermo-chemical state,  $D = D(\phi)$ , and the conditional mean diffusivity is denoted  $\tilde{D}(\mathbf{x}, t) \equiv \langle D(\phi^*[t]) | \mathbf{x} \rangle$ . For our simplified system the particle properties evolve by the following set of stochastic differential equations:

$$dX_j^*(t) = \left[ \frac{1}{\bar{\rho}} \frac{\partial}{\partial x_j} (\bar{\rho} \tilde{D}) \right]_{\mathbf{x}=\mathbf{X}^*(t),t} dt + \sqrt{2\tilde{D}(\mathbf{X}^*[t], t)} dW_j, \quad (78)$$

$$\frac{d\phi_\alpha^*(t)}{dt} = \omega(\mathbf{X}^*[t], t) [\tilde{\phi}_\alpha(\mathbf{X}^*[t], t) - \phi_\alpha^*(t)], \quad (79)$$

where  $W_j$  denotes an independent Wiener process for direction  $j$ .

For a constant mass system the particle equations (78) and (79) imply the following evolution equation for the MDF:

$$\frac{\partial F_{\phi X}^*}{\partial t} = \frac{\partial}{\partial x_j} \left[ \bar{\rho} \tilde{D} \frac{\partial}{\partial x_j} \left( F_{\phi X}^* / \bar{\rho} \right) \right] - \frac{\partial}{\partial \psi_\alpha} [F_{\phi X}^* \omega(\tilde{\phi}_\alpha - \psi_\alpha)]. \quad (80)$$

The first moment of (80) is

$$\bar{\rho} \frac{\partial \tilde{\phi}_\alpha}{\partial t} = \frac{\partial}{\partial x_j} \left( \bar{\rho} \tilde{D} \frac{\partial \tilde{\phi}_\alpha}{\partial x_j} \right), \quad (81)$$

and the SGS covariance evolves by

$$\bar{\rho} \frac{\partial}{\partial t} (\tilde{Z}_{\alpha\beta}) = \frac{\partial}{\partial x_j} \left( \bar{\rho} \tilde{D} \frac{\partial \tilde{Z}_{\alpha\beta}}{\partial x_j} \right) - 2\bar{\rho} \omega \tilde{Z}_{\alpha\beta} + 2\bar{\rho} \tilde{D} \frac{\partial \tilde{\phi}_\alpha}{\partial x_j} \frac{\partial \tilde{\phi}_\beta}{\partial x_j}. \quad (82)$$

Considering equal diffusivities, the exact transport equation for the SGS covariance (26) may be written

$$\langle \rho \rangle_\ell \frac{\partial}{\partial t} (Z_{\alpha\beta}^L) = \frac{\partial}{\partial x_j} \left( \langle \rho \rangle_\ell \langle D \rangle_L \frac{\partial Z_{\alpha\beta}^L}{\partial x_j} \right) - 2\langle \rho \rangle_\ell \langle D \rangle_L \left\langle \frac{\partial \phi_\alpha}{\partial x_j} \frac{\partial \phi_\beta}{\partial x_j} \right\rangle_L + 2\langle \rho \rangle_\ell \langle D \rangle_L \frac{\partial \langle \phi_\alpha \rangle_L}{\partial x_j} \frac{\partial \langle \phi_\beta \rangle_L}{\partial x_j}. \quad (83)$$

Hence, by comparing (82) and (83), the random walk model seems to be in excellent agreement with the exact transport equation, provided  $\omega \tilde{Z}_{\alpha\beta}$  models  $\langle D \rangle_L \langle (\partial \phi_\alpha / \partial x_j) (\partial \phi_\beta / \partial x_j) \rangle_L$ .

A problem emerges, however, when we consider the DNS limit. Using (27) the filtered dissipation term can be decomposed as follows:

$$\left\langle \frac{\partial \phi_\alpha}{\partial x_j} \frac{\partial \phi_\beta}{\partial x_j} \right\rangle_L = \left\langle \frac{\partial \langle \phi_\alpha \rangle_L}{\partial x_j} \frac{\partial \langle \phi_\beta \rangle_L}{\partial x_j} \right\rangle_L + \left\langle \frac{\partial \langle \phi_\alpha \rangle_L}{\partial x_j} \frac{\partial \phi_\beta''}{\partial x_j} \right\rangle_L + \left\langle \frac{\partial \phi_\alpha''}{\partial x_j} \frac{\partial \langle \phi_\beta \rangle_L}{\partial x_j} \right\rangle_L + \left\langle \frac{\partial \phi_\alpha''}{\partial x_j} \frac{\partial \phi_\beta''}{\partial x_j} \right\rangle_L. \quad (84)$$

Now, the important point to consider is that in the DNS limit we have  $\phi_\alpha'' \rightarrow 0$ , i.e.  $\langle \phi_\alpha \rangle_L \rightarrow \phi_\alpha$ , and consequently  $Z_{\alpha\beta}^{\text{sgs}} \rightarrow 0$  (for the model system we have  $\tilde{Z}_{\alpha\beta} \rightarrow 0$ ). Hence, in the DNS limit the last two terms in the continuous system (83) cancel, but the last term in the random walk model (82) remains, and this represents a spurious production of variance.

### 3. Numerical method

The numerical scheme presented here falls under the category of a ‘particle-mesh’ method, as described in Pope [30]. A mesh is employed for the purposes of computing and storing mean quantities. Mean particle properties are then interpolated to the particle positions.

In this section we first describe the mesh, the computation of means from the ensemble of particles, and the interpolation scheme, all of which we require for a particle-mesh method. We then describe a Strang-splitting scheme for solving (75), the particle composition evolution equation based on corrected diffusion velocities. We first develop the particle update equations. Then we provide implementation details for the method. For simplicity, we initially describe the method in the context of a single composition in 1D. The extension to multiple compositions and multiple dimensions poses no conceptual difficulties and is discussed last. The method obeys detailed conservation and guarantees individual boundedness. No time step restriction is required for stability (i.e. the method is unconditionally stable). From a modified equation analysis we show that the scheme is second-order accurate in space and time (with the time accuracy being conditional upon the grid spacing as discussed below). We also show that for a fixed grid spacing the scheme converges to a modified equation with a numerical diffusivity that is proportional to the mixing frequency,  $\omega$ . The conventional random walk/IEM approach suffers the same issue, which stems from the bias error in the mean estimate used for the IEM mixing step.

#### 3.1. Mesh

We consider a closed or periodic domain (so that the total mass is constant) of length  $L$  (see Fig. 1). The domain is subdivided into  $N_x$  uniformly spaced cells of width  $h = L/N_x$ . Following Jenny et al. [17], means are computed and stored at nodes, which in 1D double as the cell boundaries and B-spline ‘knot’ locations, labeled  $x_j$ . In what follows, particle properties for the  $i$ th particle are distinguished using the bracketed superscript ( $i$ ), discrete time locations are designated using a superscript  $n$  (without brackets), and node values are labeled with suffixes. Also note that the index summation convention does *not* apply: all summations are shown explicitly.

#### 3.2. Basis functions

In particle-mesh methods we utilize basis functions in forming mean estimates and for interpolation (both described below). Here we use a linear B-spline basis, also known as a ‘tent kernel,’

$$B(r) \equiv \begin{cases} 1 - \frac{|r|}{h} & \text{for } |r| < h, \\ 0 & \text{otherwise.} \end{cases} \quad (85)$$

When it is convenient we will use the following short-hand notation to denote basis functions centered at the knot locations (see Fig. 2),  $B_j(x) \equiv B(x - x_j)$ .

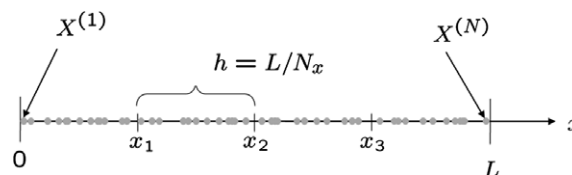


Fig. 1. Example 1D grid of length  $L$  with  $N_x = 4$  cells. Knot locations are labeled  $x_j$ . There are  $N_c$  particles per cell and  $N = N_x N_c$  particles in the domain. Particle locations are labeled consecutively from  $X^{(1)}$  to  $X^{(N)}$ .



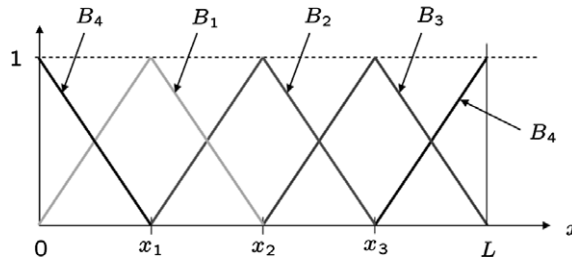


Fig. 2. Linear basis functions (see Eq. (85)) on a periodic domain with  $N_x = 4$  cells.

### 3.3. Kernel estimates of mean quantities

A particle-mesh method requires that we obtain conditional mean values of the particle properties at knot locations that can then be interpolated to the particle positions. To compute the mean property from an ensemble of particles at a certain location,  $x_j$ , we would ideally like to have a very large number of particles (samples from the MDF) all located precisely at  $x_j$ . In practice, of course, this is not the case: we have the smallest number of particles necessary to achieve the desired accuracy and they are distributed in the neighborhood of  $x_j$ . Weighted sums of these particles are used to estimate the expected value of the particle property conditional on the particle being located at  $x_j$ . These sums are known as *kernel estimates* or *cloud-in-cell* (CIC) means.

For an arbitrary particle property  $Q^*(t)$  the kernel estimate of the mean conditional on  $X^*(t) = x$  is given by [30]

$$\langle Q^*(t) | x \rangle_{N,h,w} \equiv \frac{\sum_i B(X^{(i)}[t] - x) w^{(i)}(t) Q^{(i)}(t)}{\sum_i B(X^{(i)}[t] - x) w^{(i)}(t)}, \tag{86}$$

where  $w^*$  is a weight specific to the type of mean estimate being computed. For example, the estimate could be “mass-weighted,” in which case one would use the particle mass as the weighting factor,  $w^* = m^*$ . Other weighting factors are used later in the paper.

There are two types of error associated with the estimate (86). The first is random statistical error, which decreases (slowly) as the number of particles is increased. This error stems from randomness in the particle positions and from the practical necessity of using a finite number of particles to form the estimate. In what follows we will assume that the particle positions are sampled from a uniform distribution (a requirement for constant density flows, which we consider in Section 4) and that a sufficient number of particles is being used such that the statistical error is small relative the deterministic error, which is known as the *bias*. The bias error is defined as the difference between the expectation of the mean estimate and the true conditional mean,

$$\beta_Q(x, t) \equiv \langle \langle Q^*(t) | x \rangle_{N,h,w} \rangle - \langle Q^*(t) | x \rangle. \tag{87}$$

The bias error increases with the mesh spacing  $h$ , and for the simple case of uniform weights,  $w^*$ , we have (specifically for the tent kernel in 1D [30])

$$\beta_Q = \frac{h^2}{12} \frac{\partial^2 \langle Q^* | x \rangle}{\partial x^2} + \mathcal{O}(h^4). \tag{88}$$

In the more general case of nonuniform weights the bias is more complicated, and depends on spatial derivatives of  $\langle w^* | x \rangle$ . The leading term is still  $\mathcal{O}(h^2)$ , however, owing to symmetry of the kernel.

### 3.4. Interpolation

In particle-mesh methods the particle mean  $Q^{(i)}$  at the particle position  $X^{(i)}$  is obtained by interpolation. Here we use (85) as a linear basis and the resulting B-spline, which is second-order accurate in space, is given by

$$Q^{(i)} = \sum_j B_j(X^{(i)}) Q_j, \quad (89)$$

where  $Q_j$  is the particle property at the  $j$ th knot. It is to be noted that, based on the analysis of Jenny et al. [17], one of the requirements for detailed conservation in the implementation of the IEM model is that the basis functions used in the kernel estimate and the interpolation scheme must be the same (this is further discussed in Section 3.5.4 below).

### 3.5. A Strang-splitting scheme

Our goal is to integrate (75) from  $t^n$  to  $t^{n+1} \equiv t^n + \Delta t$ . Without loss of generality we may write the scheme in terms of a single composition and so we drop the species index. Let  $\phi^{*,n}$  represent the initial composition for a general particle on a given time step and let  $s_k$  represent discrete states in the time step subcycle. We consider a Strang-splitting with the following substeps:

1. IEM for  $\frac{1}{2}\Delta t : \phi^{*,n} \rightarrow \phi^{*,s_1}$ .
2. Spatial transport for  $\Delta t : \phi^{*,s_1} \rightarrow \phi^{*,s_2}$ .
3. IEM for  $\frac{1}{2}\Delta t : \phi^{*,s_2} \rightarrow \phi^{*,n+1}$ .

We first describe the development of the scheme in terms of a general particle and find a simplified particle update equation. Then we discuss precise implementation details for particle evolution.

#### 3.5.1. Development of a one-step update

Here we give an overview of the methods used in the three substeps and show that they can be combined into a one-step update to the particle composition.

To avoid a timestep restriction the IEM model is intergrated analytically using frozen values of the mean and mixing rate. In the first substep these values are fixed at the  $n$ th time level. Let  $\hat{\phi}^{*,n}$  and  $\omega^{*,n}$  represent the CIC mean and mixing rate, respectively, at the particle position at  $t^n$ . The first IEM substep yields

$$\phi^{*,s_1} = \phi^{*,n} + c^{*,n}(\hat{\phi}^{*,n} - \phi^{*,n}), \quad (90)$$

where the “decay-factor” is here defined as

$$c^{*,n} \equiv 1 - \exp(-\omega^{*,n}\Delta t/2). \quad (91)$$

In the second substep, the mean transport equation

$$\frac{\partial \tilde{\phi}}{\partial t} = \frac{1}{\bar{\rho}} \frac{\partial}{\partial x} \left( \bar{\rho} \tilde{D} \frac{\partial \tilde{\phi}}{\partial x} \right) \quad (92)$$

is integrated numerically for a time interval  $\Delta t$  from the initial condition  $\hat{\phi}^{*,n}$ . To avoid a time step restriction, this is done using a Crank–Nicolson scheme, described below. The particle composition is then advanced by

$$\phi^{*,s_2} = \phi^{*,s_1} + \Delta \hat{\phi}^*. \quad (93)$$

where  $\Delta \hat{\phi}^*$  denotes the increment in the numerical solution to (92) evaluated at the particle position.

In the final IEM substep the mean, defined by  $\hat{\phi}^{*,+} \equiv \hat{\phi}^{*,n} + \Delta \hat{\phi}^*$ , and mixing rate are frozen at the  $n+1$  time level and  $\phi^{*,s_2}$  is used as the initial condition. We denote the mean for this substep by  $\hat{\phi}^{*,+}$  instead of  $\hat{\phi}^{*,n+1}$  because it is not obtained from a CIC estimate using particle compositions at time  $t^{n+1}$ , which would not precisely equal  $\hat{\phi}^{*,+}$ . The resulting particle update is

$$\phi^{*,n+1} = \phi^{*,s_2} + c^{*,n+1}(\hat{\phi}^{*,+} - \phi^{*,s_2}), \quad (94)$$

where

$$c^{*,n+1} \equiv 1 - \exp(-\omega^{*,n+1}\Delta t/2). \quad (95)$$

By manipulating (90), (93) and (94) we arrive at the following one-step particle update for the Strang-splitting scheme,

$$\phi^{*,n+1} = \phi^{*,n} + \Delta \hat{\phi}^* + \tilde{c}^* (\hat{\phi}^{*,n} - \phi^{*,n}), \tag{96}$$

where the “effective decay-factor” is given by

$$\tilde{c}^* = c^{*,n} + c^{*,n+1} - c^{*,n} c^{*,n+1}. \tag{97}$$

Note that the overall scheme is unconditionally stable by construction, because each substep of the Strang-splitting is unconditionally stable.

### 3.5.2. Details of the particle-mesh method

In this section, we provide details pertaining to the particle-mesh method where certain values are obtained or computed at knot locations and then interpolated to the particle positions to obtain the final particle update equation.

Recall that the mixing rate field is obtainable from a separate part of the LES formulation, which we are not addressing. Defining  $\omega_j^n \equiv \omega(x_j, t^n)$  and  $\omega_j^{n+1} \equiv \omega(x_j, t^{n+1})$ , the decay-factors for the IEM substeps at the knot locations are

$$c_j^n \equiv 1 - \exp(-\omega_j^n \Delta t / 2), \tag{98}$$

and

$$c_j^{n+1} \equiv 1 - \exp(-\omega_j^{n+1} \Delta t / 2). \tag{99}$$

The effective decay-factor at the  $j$ th knot becomes

$$\tilde{c}_j \equiv c_j^n + c_j^{n+1} - c_j^n c_j^{n+1}, \tag{100}$$

$$= 1 - \exp(-\tilde{\omega}_j \Delta t), \tag{101}$$

where

$$\tilde{\omega}_j \equiv \frac{1}{2} (\omega_j^n + \omega_j^{n+1}). \tag{102}$$

As shown by the analysis of Jenny et al. [17] and also below (Section 3.5.4), for the scheme to obey detailed conservation the mean estimate must be formed using a mass/decay-factor weighting. Here we consider arbitrary mass weightings, which are needed in practice for variable-density flows, even though the particle masses are equal for the test problems we present in Section 4. The CIC mean at the  $j$ th knot at time  $t^n$  is given by

$$\hat{\phi}_j^n \equiv \langle \phi^*(t^n) | X^*(t^n) = x_j \rangle_{N,h,m,\tilde{c}} = \frac{\sum_i B_j(X^{(i),n}) m^{(i)} \tilde{c}^{(i)} \phi^{(i),n}}{\sum_i B_j(X^{(i),n}) m^{(i)} \tilde{c}^{(i)}}, \tag{103}$$

where  $\tilde{c}^{(i)}$  is obtained by linear interpolation using (101) and (89).

The knot values of the CIC means and the mean shifts (discussed in detail below) are interpolated to the particle positions to obtain  $\hat{\phi}^{(i),n}$ , and  $\Delta \hat{\phi}^{(i)}$ , respectively. Finally, the particle update equation for the Strang-splitting scheme is given by

$$\phi^{(i),n+1} = \phi^{(i),n} + \Delta \hat{\phi}^{(i)} + \tilde{c}^{(i)} (\hat{\phi}^{(i),n} - \phi^{(i),n}). \tag{104}$$

### 3.5.3. Mean shift

With  $h$  being uniform, the mean particle mass density at the  $j$ th knot may be written as

$$\bar{\rho}(x_j, t) = \frac{\hat{m}_j(t)}{h} + \mathcal{O}(h^2), \tag{105}$$

where the “knot mass” is given by

$$\hat{m}_j(t) \equiv \sum_i B_j(X^{(i)}[t])m^{(i)}. \tag{106}$$

It is assumed that particle diffusion is to be implemented into the overall LES scheme in a fractional step where the particle positions remain fixed. Thus, the knot mass remains constant during the time step.

The CIC estimate of the mean diffusivity at the  $j$ th knot is computed by

$$\hat{D}_j(t) = \frac{\sum_i B_j(X^{(i)}[t])m^{(i)}D(\phi^{(i)}[t])}{\sum_i B_j(X^{(i)}[t])m^{(i)}}. \tag{107}$$

To achieve second-order temporal accuracy we require the diffusivity to be centered in time. Even with the particle positions frozen for the given time step, linear interpolation between  $\hat{D}_j^n$  and  $\hat{D}_j^{n+1}$  would require a nonlinear solution procedure, because we require  $\phi^*(t^{n+1})$  to evaluate  $\hat{D}_j^{n+1}$ . To avoid this difficulty, we use an Adams–Bashforth extrapolation,

$$\hat{D}_j^{n+1/2} = \frac{3}{2}\hat{D}_j^n - \frac{1}{2}\hat{D}_j^{n-1}, \tag{108}$$

which is second-order accurate in time.

Let  $x_{j\pm 1/2}$  denote the face locations of a control-volume (CV) centered at the knot location  $x_j$ . Given the knot mass and the time-centered diffusivity, a Crank–Nicolson/finite-volume (FV) scheme to solve (92), which is second-order in space and time, is

$$\frac{\hat{\phi}_j^+ - \hat{\phi}_j^n}{\Delta t} = \frac{1}{\hat{m}_j h} \left[ \hat{m}_{j+1/2} \hat{D}_{j+1/2}^{n+1/2} \left( \frac{\delta \hat{\phi}}{\delta x} \right)_{j+1/2}^{n+1/2} - \hat{m}_{j-1/2} \hat{D}_{j-1/2}^{n+1/2} \left( \frac{\delta \hat{\phi}}{\delta x} \right)_{j-1/2}^{n+1/2} \right]. \tag{109}$$

The face values of the mass and diffusivity are obtained by linear interpolation,

$$\hat{m}_{j+1/2} = \frac{1}{2}[\hat{m}_j + \hat{m}_{j+1}] \tag{110}$$

and

$$\hat{D}_{j+1/2}^{n+1/2} = \frac{1}{2}[\hat{D}_j^{n+1/2} + \hat{D}_{j+1}^{n+1/2}]. \tag{111}$$

The gradients at the CV faces are given by,

$$\left( \frac{\delta \hat{\phi}}{\delta x} \right)_{j+1/2}^{n+1/2} = \frac{\hat{\phi}_{j+1}^{n+1/2} - \hat{\phi}_j^{n+1/2}}{h}, \tag{112}$$

where compositions at the midpoint of the time interval are

$$\hat{\phi}_j^{n+1/2} = \frac{1}{2}[\hat{\phi}_j^+ + \hat{\phi}_j^n]. \tag{113}$$

The values of  $\hat{\phi}_j^+$  are found implicitly.

The update of the means can now be written as

$$\hat{\phi}_j^+ - \hat{\phi}_j^n \equiv \Delta \hat{\phi}_j = \Delta t \sum_k A_{jk} \hat{\phi}_k^{n+1/2}, \tag{114}$$

where the  $N_x \times N_x$  matrix  $\mathbf{A}$  is tridiagonal with elements

$$A_{k-1,k} = \frac{\hat{m}_{k-1/2} \hat{D}_{k-1/2}^{n+1/2}}{\hat{m}_j h^2}, \tag{115}$$

$$A_{k+1,k} = \frac{\hat{m}_{k+1/2} \hat{D}_{k+1/2}^{n+1/2}}{\hat{m}_j h^2}, \tag{116}$$

$$A_{k,k} = -(A_{k-1,k} + A_{k+1,k}). \tag{117}$$

Rearranging (114) results in the following Crank–Nicolson scheme for the mean shift,

$$\left[ \mathbf{I} - \frac{\Delta t}{2} \mathbf{A} \right] \Delta \hat{\phi} = [\Delta t \mathbf{A}] \hat{\phi}^n, \tag{118}$$

where  $\mathbf{I}$  is the identity matrix and  $\hat{\phi}^n$  and  $\Delta \hat{\phi}$  are  $N_x$ -vectors with elements  $\hat{\phi}_j^n$  and  $\Delta \hat{\phi}_j$ , respectively.

### 3.5.4. Detailed conservation

Detailed conservation requires

$$\sum_i m^{(i)} \phi^{(i),n+1} = \sum_i m^{(i)} \phi^{(i),n}. \tag{119}$$

Multiplying (104) by  $m^{(i)}$  and summing over all particles we find that the following are sufficient conditions to ensure that (119) is satisfied:

$$\sum_i m^{(i)} \Delta \hat{\phi}^{(i)} = 0, \tag{120}$$

$$\sum_i m^{(i)} \tilde{c}^{(i)} (\hat{\phi}^{(i),n} - \phi^{(i),n}) = 0. \tag{121}$$

Because of the following identity,

$$\sum_i m^{(i)} \Delta \hat{\phi}^{(i)} = \sum_i m^{(i)} \left[ \sum_j B_j(X^{(i)}) \Delta \hat{\phi}_j \right] = \sum_j \left[ \sum_i B_j(X^{(i)}) m^{(i)} \right] \Delta \hat{\phi}_j = \sum_j \hat{m}_j \Delta \hat{\phi}_j, \tag{122}$$

the first condition (120) is equivalent to  $\sum_j \hat{m}_j \Delta \hat{\phi}_j = 0$ . By rearranging (114) and summing over the columns  $j$ , we find

$$\sum_j \hat{m}_j \Delta \hat{\phi}_j = \frac{\Delta t}{h^2} \sum_j \sum_k A_{jk} \hat{\phi}_k^{n+1/2} = 0, \tag{123}$$

since the columns of  $\mathbf{A}$  sum to zero, as is evident from (115)–(117). Thus, the satisfaction of (120) is proved, and it is to be noted that (123) holds for any specification of  $\hat{\phi}_k^n$ .

We now show, as asserted earlier, that the definition of  $\hat{\phi}_j^n$  by (103) leads to the satisfaction of (121). With  $\hat{\phi}^{(i),n}$  determined from (89), we can rewrite (121) as

$$\begin{aligned} \sum_i m^{(i)} \tilde{c}^{(i)} (\hat{\phi}^{(i),n} - \phi^{(i),n}) &= \sum_i m^{(i)} \tilde{c}^{(i)} \left[ \sum_j B_j(X^{(i)}) \hat{\phi}_j^n \right] - \sum_i m^{(i)} \tilde{c}^{(i)} \phi^{(i),n} \\ &= \sum_j \left[ \sum_i B_j(X^{(i)}) m^{(i)} \tilde{c}^{(i)} \right] \hat{\phi}_j^n - \sum_i m^{(i)} \tilde{c}^{(i)} \phi^{(i),n} \\ &= \sum_j \left[ \sum_i B_j(X^{(i)}) m^{(i)} \tilde{c}^{(i)} \phi^{(i),n} \right] - \sum_i m^{(i)} \tilde{c}^{(i)} \phi^{(i),n} \\ &= \sum_i \underbrace{\left[ \sum_j B_j(X^{(i)}) \right]}_1 m^{(i)} \tilde{c}^{(i)} \phi^{(i),n} - \sum_i m^{(i)} \tilde{c}^{(i)} \phi^{(i),n} = 0. \end{aligned} \tag{124}$$

Notice that (103) is invoked in going from the second to the third line, and the normalization property of the basis function is exploited in the last step. This proves that (121) is satisfied. Thus, the present scheme satisfies detailed conservation.

### 3.5.5. Realizability

As mentioned previously, in the continuous system the realizability constraint  $\sum_{\alpha=1}^{n_s} \phi_\alpha = 1$  requires the diffusive fluxes to sum to zero. This constraint is implemented in the numerical method by requiring the sum of the knot mean shifts to be zero. First we show that this is indeed a necessary and sufficient condition

for realizability given the particle update (104). We then show that the required adjustments to the mean shift do not affect the conservation properties of the scheme.

Given  $\sum_{\alpha=1}^{n_s} \phi_{\alpha}^{(i),n} = 1$  for all particles  $i$ , realizability dictates that  $\sum_{\alpha=1}^{n_s} \phi_{\alpha}^{(i),n+1} = 1$  for all particles  $i$ . A necessary and sufficient condition for this to hold is to have  $\sum_{\alpha=1}^{n_s} \Delta \hat{\phi}_{\alpha,j} = 0$  at each knot  $j$ . We now show this to be true: summing (104) over species gives

$$\sum_{\alpha=1}^{n_s} \phi_{\alpha}^{(i),n+1} = \underbrace{\sum_{\alpha=1}^{n_s} \phi_{\alpha}^{(i),n}}_1 + \sum_{\alpha=1}^{n_s} \Delta \hat{\phi}_{\alpha}^{(i)} + \tilde{c}^{(i)} \left[ \underbrace{\sum_{\alpha=1}^{n_s} \hat{\phi}_{\alpha}^{(i),n}}_1 - \underbrace{\sum_{\alpha=1}^{n_s} \phi_{\alpha}^{(i),n}}_1 \right]. \tag{125}$$

Note that the first and last summations on the RHS of (125) are given as unity. The third summation is also unity since

$$\sum_{\alpha=1}^{n_s} \hat{\phi}_{\alpha}^{(i),n} = \sum_{\alpha=1}^{n_s} \sum_j B_j(X^{(i)}) \hat{\phi}_{\alpha,j}^n = \sum_j B_j(X^{(i)}) \underbrace{\left[ \sum_{\alpha=1}^{n_s} \hat{\phi}_{\alpha,j}^n \right]}_1 = \sum_j B_j(X^{(i)}) = 1. \tag{126}$$

The third step in (126) follows from

$$\sum_{\alpha=1}^{n_s} \hat{\phi}_{\alpha,j}^n = \sum_{\alpha=1}^{n_s} \left[ \frac{\sum_i B_j(X^{(i)}) m^{(i)} \tilde{c}^{(i)} \phi_{\alpha}^{(i),n}}{\sum_i B_j(X^{(i)}) m^{(i)} \tilde{c}^{(i)}} \right] = \frac{\sum_i B_j(X^{(i)}) m^{(i)} \tilde{c}^{(i)} \underbrace{\left[ \sum_{\alpha=1}^{n_s} \phi_{\alpha}^{(i),n} \right]}_1}{\sum_i B_j(X^{(i)}) m^{(i)} \tilde{c}^{(i)}} = 1. \tag{127}$$

Thus, from (125), realizability requires  $\sum_{\alpha=1}^{n_s} \Delta \hat{\phi}_{\alpha}^{(i)} = 0$ . The necessary and sufficient condition for this to hold is that the knot mean shifts sum to zero:

$$\sum_{\alpha=1}^{n_s} \Delta \hat{\phi}_{\alpha}^{(i)} = \sum_{\alpha=1}^{n_s} \sum_j B_j(X^{(i)}) \Delta \hat{\phi}_{\alpha,j} = \sum_j B_j(X^{(i)}) \left[ \sum_{\alpha=1}^{n_s} \Delta \hat{\phi}_{\alpha,j} \right] = 0 \quad \text{for any } X^{(i)} \text{ iff } \sum_{\alpha=1}^{n_s} \Delta \hat{\phi}_{\alpha,j} = 0 \text{ for all } j. \tag{128}$$

Since the mean shifts obtained from the FV scheme are not guaranteed to satisfy realizability we require the following correction. With a slight change in notation, let  $\Delta \hat{\phi}_{\alpha,j}^{\text{FV}}$  be the knot mean shift obtained from the Crank–Nicolson/FV scheme; i.e. the result from (109). The corrected knot mean shifts are obtained from

$$\Delta \hat{\phi}_{\alpha,j} = \Delta \hat{\phi}_{\alpha,j}^{\text{FV}} - \frac{1}{n_s} \sum_{\beta=1}^{n_s} \Delta \hat{\phi}_{\beta,j}^{\text{FV}}. \tag{129}$$

Note that this correction does not affect the conservation properties of the scheme since by utilizing (123) we have

$$\sum_j \hat{m}_j \Delta \hat{\phi}_{\alpha,j} = \sum_j \hat{m}_j \left( \Delta \hat{\phi}_{\alpha,j}^{\text{FV}} - \frac{1}{n_s} \sum_{\beta=1}^{n_s} \Delta \hat{\phi}_{\beta,j}^{\text{FV}} \right) = \underbrace{\sum_j \hat{m}_j \Delta \hat{\phi}_{\alpha,j}^{\text{FV}}}_0 - \frac{1}{n_s} \sum_{\beta=1}^{n_s} \underbrace{\left[ \sum_j \hat{m}_j \Delta \hat{\phi}_{\beta,j}^{\text{FV}} \right]}_0 = 0. \tag{130}$$

Thus, (120) is satisfied.

The correction (129) effectively enforces the constraint that the diffusion velocities must sum to zero. Hence, as mentioned, the numerical method is solving (75), the particle evolution model written in terms of the corrected diffusion velocity.

### 3.5.6. Boundedness

Given  $\phi^{(i),n} \leq \phi_{\max}^n$  and  $\tilde{c}^{(i)} \leq 1$ , (104) yields

$$\phi^{(i),n+1} \leq \phi_{\max}^n + \Delta \hat{\phi}^{(i)} + \tilde{c}^{(i)} (\hat{\phi}^{(i),n} - \phi_{\max}^n). \tag{131}$$

Thus,  $\phi^{(i),n+1}$  does not exceed the maximum bound  $\phi_{\max}^n$  provided that

$$\Delta \hat{\phi}^{(i)} + \tilde{c}^{(i)} (\hat{\phi}^{(i),n} - \phi_{\max}^n) \leq 0. \tag{132}$$

From (132) we see that if  $\hat{\phi}^{(i),n} = \phi_{\max}^n$  boundedness requires  $\Delta\hat{\phi}^{(i)} \leq 0$  independent of  $\tilde{c}^{(i)}$ . We now show that this is guaranteed to be true: with  $X^{(i),n} \in [x_j, x_{j+1}]$ , due to linear interpolation  $\hat{\phi}^{(i),n} = \phi_{\max}^n$  iff  $\hat{\phi}_j^n = \hat{\phi}_{j+1}^n = \phi_{\max}^n$ . The Crank–Nicolson/finite-volume scheme ensures that  $\hat{\phi}_j^+ \leq \phi_{\max}^n$  and  $\hat{\phi}_{j+1}^+ \leq \phi_{\max}^n$ . Thus,  $\Delta\hat{\phi}_j \equiv \hat{\phi}_j^+ - \hat{\phi}_j^n = \hat{\phi}_j^+ - \phi_{\max}^n \leq 0$  and  $\Delta\hat{\phi}_{j+1} \equiv \hat{\phi}_{j+1}^+ - \hat{\phi}_{j+1}^n = \hat{\phi}_{j+1}^+ - \phi_{\max}^n \leq 0$ . Hence,  $\Delta\hat{\phi}^{(i)} \leq 0$  is guaranteed due to linear interpolation. Therefore, the case where  $\hat{\phi}^{(i),n} = \phi_{\max}^n$  does not require special treatment of the decay-factor to ensure boundedness.

Eq. (132) can be rewritten as

$$\tilde{c}^{(i)} \geq \frac{\Delta\hat{\phi}^{(i)}}{\phi_{\max}^n - \hat{\phi}^{(i),n}}. \tag{133}$$

The analogous argument for the minimum bound leads to

$$\tilde{c}^{(i)} \geq \frac{\Delta\hat{\phi}^{(i)}}{\phi_{\min}^n - \hat{\phi}^{(i),n}}. \tag{134}$$

With  $\tilde{c}^{(i)}$  being interpolated onto the particles via (89), a sufficient condition to satisfy (133) and (134) is

$$\tilde{c}_j \geq \tilde{c}_j^{\min} \equiv \max_k \left( \left[ \frac{\Delta\hat{\phi}_k}{\phi_{\min}^n - \hat{\phi}_k^n} \right], \left[ \frac{\Delta\hat{\phi}_k}{\phi_{\max}^n - \hat{\phi}_k^n} \right] \right) \text{ for } k = \{j-1, j, j+1\}, \tag{135}$$

where  $\Delta\hat{\phi}_k$  are the knot mean shifts that have been corrected via (129). Note that (135) is the discrete analog of the mixing rate bound (57). We require (57) to be satisfied to form a well-posed problem, but this does not guarantee satisfaction of (135), which is necessary to guarantee boundedness of the discrete system.

Since  $\tilde{c}^{(i)}$  is needed to compute  $\hat{\phi}_j^n$  and the initially computed decay-factors are not guaranteed to satisfy (135), determination of the final CIC mean requires a two-step procedure. We first compute the CIC mean using (89), (101) and (103) based on the specified mixing rate. Then the mean shift is computed using (109). If necessary, the decay-factors are then adjusted to satisfy (135), i.e. if  $\tilde{c}_j < \tilde{c}_j^{\min}$  then we set  $\tilde{c}_j = \tilde{c}_j^{\min}$ . New CIC means  $\hat{\phi}_j^n$  are then computed at the knots and interpolated to the particle positions to be used in (104). Note that, within the spatial truncation error of the scheme, the mean shift is unaffected by the variation in the decay-factor. Also, the decay-factor does not affect the conservation properties of the mean shift. Hence, there is no need to recompute the mean shift based on the corrected CIC means. Details of this procedure are provided below.

### 3.5.7. Algorithmic details and computational cost

A step-by-step summary of the algorithm is given below in Algorithm 1. An approximate cost for the algorithm is given in Table 1 assuming that the values of the basis functions at the particle positions are computed once and stored. Hence, the cost estimates are for a best-case cost scenario with worst case storage.

**Algorithm 1.** Particle diffusion 1D. **Goal:** Find  $\phi^*(t^{n+1})$ .

1. **Given:**  $\phi^*(t^n)$ ,  $X^*(t^n)$ ,  $m^*$ ,  $D(\phi)$ ,  $\hat{D}_j^{n-1}$  and  $\omega(x,t)$ .
2. Compute  $\tilde{\omega}_j$  from (102).
3. Compute  $\tilde{c}_j$  from (101).
4. Compute and store the basis functions for each particle  $B_j(X^{(i)})$  using (85).
5. Compute  $\hat{m}_j$  from (106) and store  $B_j(X^{(i)})m^{(i)}$ .
6. Compute  $\hat{D}_j^n$  from (107).
7. Compute  $\hat{D}_j^{n+1/2}$  from (108).
8. Interpolate knot decay-factors  $\tilde{c}_j$  to particle positions using (89) to obtain  $\tilde{c}^{(i)}$ .
9. Compute CIC means at knots  $\hat{\phi}_j^n$  from (103).
10. Compute face values of the knot masses  $\hat{m}_{j+1/2}$  from (110).
11. Compute face values of the knot diffusivities  $\hat{D}_{j+1/2}^{n+1/2}$  from (111).
12. Build the **A** matrix using (115)–(117).
13. Build the source vector for the linear solve  $[\Delta t \mathbf{A}] \hat{\phi}^n$ .

14. Build the tridiagonal matrix  $[\mathbf{I} - \frac{\Delta t}{2} \mathbf{A}]$ .
15. Solve for the knot mean shifts  $\Delta \hat{\phi}_j^{\text{EV}}$  from (109). (This is simply the solution of a tridiagonal system and can be computed directly using the Thomas algorithm [2,15].)
16. Correct mean shifts for realizability via (129) to obtain  $\hat{\phi}_j$ .
17. Check and, if necessary, adjust knot decay factors to satisfy (135); i.e. if  $\tilde{c}_j < \tilde{c}_j^{\text{min}}$ , then set  $\tilde{c}_j = \tilde{c}_j^{\text{min}}$ .
18. For the affected cells, interpolate new decay factors to particle positions using (89) and  $\tilde{c}_j$  obtained from Step 1.
19. Recompute CIC means at the knots  $\hat{\phi}_j^n$  from (103) using  $\tilde{c}^{(i)}$  obtained from Step 1.
20. Interpolate CIC means to particle positions using (89) to obtain  $\hat{\phi}^{(i),n}$ .
21. Interpolate mean shift to particle positions using (89) to obtain  $\Delta \hat{\phi}^{(i)}$ .
22. Update particle compositions using (104) to obtain  $\phi^{(i),n+1}$ .
23. **Done.**

The complexity of computing  $D_x(\phi)$  is an uncertainty in the cost estimate. The typical method of computing “mixture-averaged” or “effective” diffusivities for gas mixtures (see, e.g. [41]) is  $\mathcal{O}(n_\phi)$  for each composition. And therefore we estimate this cost as  $\mathcal{O}(n_\phi^2 N)$  in Table 1. However, in practice one could group compositions with similar properties, thereby significantly reducing the cost of evaluating the diffusivities.

If we consider a practical calculation where there are a significant number of compositions (say  $n_\phi \approx 10$ ) and a significant number of particles per cell (say  $N_c \approx 40$ ) then the cost of the algorithm is dominated by the computation of CIC means and interpolation. Thanks to the ADI algorithm (see Section 3.6.1 below), for square or cubic computational domains the grid-based cost scales like  $N_x^D$ , where  $D$  is the spatial dimension. A detailed operation count for the multi-dimensional case reveals that the ratio of particle work to grid-based work remains roughly constant.

Table 1  
Computational cost for Algorithm 1

Step	$N_x$ , +/-	$N_x$ , × or /	$N_x$ , exp	$N_x$ , logical	$N$ , +/-	$N$ , × or /	$N$ , $D_x(\phi)$	Comment
2	1	1						
3	1	1	1					
4					2	2		
5	-1				2	2		
6	$-n_\phi$	$n_\phi$			$2n_\phi$	$2n_\phi$	$n_\phi^2$	
7	$n_\phi$	$2n_\phi$						
8					1	2		
9	$-2n_\phi$	$n_\phi$			$4n_\phi$	$4n_\phi$		
10	1	1						
11	$n_\phi$	$n_\phi$						
12	$n_\phi$	$4n_\phi + 1$						
13	$2n_\phi$	$4n_\phi$						
14	$n_\phi$	$3n_\phi$						
15	$4n_\phi$	$5n_\phi$						
16	$2n_\phi - 1$	1						
17	$2n_\phi$	$2n_\phi$		$6n_\phi$				
18					1	2		Worst case
19	$-2n_\phi$	$n_\phi$			$4n_\phi$	$4n_\phi$		Worst case
20					$n_\phi$	$2n_\phi$		
21					$n_\phi$	$2n_\phi$		
22					$3n_\phi$	$n_\phi$		
Total	$5n_\phi + 1$	$19n_\phi + 5$	1	$6n_\phi$	$15n_\phi + 6$	$15n_\phi + 8$	$n_\phi^2$	

The first column cross-references this table with the line number in Algorithm 1, above. The next four columns give the cost per grid node for: additions or subtractions (+/-), multiplications or divisions (× or /), exponential operations (exp), and logical operations (logical). Recall that  $n_\phi$  is the number of compositions in the simulation. The next three columns show the operation count per particle for: additions or subtractions, multiplications or divisions, and diffusivity evaluations. Note that the negative values in the first column are due to, e.g. needing  $2N_c - 1$  additions per knot to form a CIC mean.



### 3.5.8. Simple modified equation

Here we present the modified equation for the Strang-splitting scheme for the simplified case of a single composition, and of constant and uniform density, diffusivity, and mixing rate in 1D. This case is sufficient to illustrate some important properties of the scheme which are further discussed in the results section to follow. For this case, the model equation for the particle composition (68) reduces to

$$\frac{d\phi^*}{dt} = D \frac{\partial^2 \tilde{\phi}}{\partial x^2} + \omega(\tilde{\phi} - \phi^*). \tag{136}$$

or equivalently

$$\phi_t^* = D\tilde{\phi}_{xx} + \omega(\tilde{\phi} - \phi^*), \tag{137}$$

where we use the more compact notation in which the subscripts  $t$  and  $x$  denote temporal and spatial derivatives. In these equations  $\phi^*(t)$  is the particle property,  $\tilde{\phi}$  is the conditional mean of  $\phi^*(t)$  and  $\tilde{\phi}_{xx}$  is its second spatial derivative.

An analysis of the scheme shows that in the numerical implementation the particle composition evolves by the modified equation

$$\phi_t^* = D\tilde{\phi}_{xx} + \omega(\tilde{\phi} - \phi^*) + \frac{Dh^2}{6}\tilde{\phi}_{xxxx} + \frac{\omega h^2}{12}\tilde{\phi}_{xx} - \frac{\Delta t h^2}{24}(\omega^2\tilde{\phi}_{xx} + \omega D\tilde{\phi}_{xxxx}) + \mathcal{O}(\Delta t^2) + \mathcal{O}(h^4). \tag{138}$$

It may be seen that the first three terms correspond to the model equation (137), so that the remaining terms represent the truncation error. The leading order truncation errors are of order  $h^2$  and  $\Delta t^2$  provided that  $h^2/\Delta t$  remains bounded as  $\Delta t$  tends to zero. Thus, the scheme is consistent, second-order accurate in space, and second-order accurate in time under the condition that the spatial truncation error is not dominant.

### 3.6. Extension to multiple dimensions

The power of the B-spline representation becomes readily apparent as we extend the method to higher dimensions. Here we show the extension to the two-dimensional (2D) case. Hopefully, the pattern for 3D will then be clear.

In principle, particle methods can be mesh free. Not surprisingly then, the particle update equation for the multi-dimensional case is identical to the 1D case, which we reiterate here,

$$\phi^{(i),n+1} = \phi^{(i),n} + \Delta\hat{\phi}^{(i)} + \tilde{c}^{(i)}(\hat{\phi}^{(i),n} - \phi^{(i),n}). \tag{139}$$

The differences simply come in interpolation, CIC mean estimation, and solution of the knot mean shift.

Here, for simplicity in introducing the concepts, we consider a square domain of side  $L$ , and a uniform mesh of spacing  $h = L/N_x$ , where  $N_x$  is the number of cells in each direction. Knot locations are given by  $(x_j, y_k) = (jh, kh)$  with  $j = 1:N_x$  and  $k = 1:N_x$  (see Fig. 3).

The interpolation operation in 2D is simply

$$Q^{(i)} = \sum_j \sum_k B_j(X^{(i)})B_k(Y^{(i)})Q_{jk}, \tag{140}$$

where  $Q_{jk}$  represents data stored on the mesh at knot location  $(x_j, y_k)$  and  $Q^{(i)}$  is the interpolated value at the  $i$ th particle location  $(X^{(i)}, Y^{(i)})$ . Hence, the values of  $\Delta\hat{\phi}^{(i)}$ ,  $\tilde{c}^{(i)}$  and  $\hat{\phi}^{(i),n}$  in (139) are obtained using (140) based on the knot values  $\Delta\hat{\phi}_{jk}$ ,  $\tilde{c}_{jk}$  and  $\hat{\phi}_{jk}^n$ , respectively.

The effective decay-factor at knot  $(j, k)$  is

$$\tilde{c}_{jk} \equiv 1 - \exp(-\tilde{\omega}_{jk}\Delta t), \tag{141}$$

where

$$\tilde{\omega}_{jk} \equiv \frac{1}{2}[\omega(x_j, y_k, t^n) + \omega(x_j, y_k, t^{n+1})]. \tag{142}$$

The decay-weighted CIC mean is given by

$$\hat{\phi}_{jk}^n \equiv \frac{\sum_i B_j(X^{(i)})B_k(Y^{(i)})m^{(i)}\tilde{c}^{(i)}\phi^{(i),n}}{\sum_i B_j(X^{(i)})B_k(Y^{(i)})m^{(i)}\tilde{c}^{(i)}}. \tag{143}$$

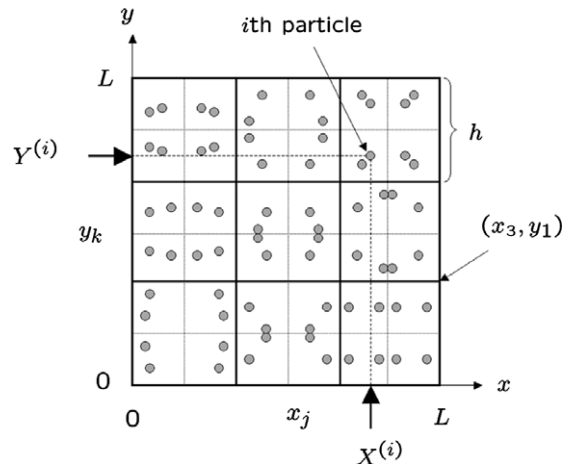


Fig. 3. A 2D square domain of side  $L$  with a uniform grid of spacing  $h = L/N_x$  (for  $N_x = 3$ ). The knot locations are labelled  $(x_j, y_j)$  and as an example we point to  $(x_3, y_1)$ . The number of particles in each cell in this example is  $N_c = 8$ . The position of the  $i$ th particle is labelled  $(X^{(i)}, Y^{(i)})$ . In a given cell the particle positions are selected from a uniform random distribution in one quadrant of the cell for  $N_c/4$  particles. The remaining particle positions are specified by mirror reflections about the lines which divide the cell into quadrants. This results in uniform knot masses, computed via (144), throughout the domain.

The knot mass is defined to be

$$\hat{m}_{jk} \equiv \sum_i B_j(X^{(i)})B_k(Y^{(i)})m^{(i)}, \tag{144}$$

and the CIC mean diffusivity is computed by

$$\hat{D}_{jk}(t) = \frac{\sum_i B_j(X^{(i)})B_k(Y^{(i)})m^{(i)}D(\phi^{(i)}[t])}{\sum_i B_j(X^{(i)})B_k(Y^{(i)})m^{(i)}}. \tag{145}$$

For the purpose of mapping the physical grid locations to the ordering in computational space we use a lexicographical ordering such that the solution vector index  $p$  is mapped to the knot  $(j, k)$  by

$$p = j + (k - 1)N_x. \tag{146}$$

After the mapping, the linear system for the 2D Crank–Nicolson/finite-volume scheme can be written in the same form as 1D system,

$$\left[ \mathbf{I} - \frac{\Delta t}{2} \mathbf{A} \right] \Delta \hat{\phi} = [\Delta t \mathbf{A}] \hat{\phi}^n, \tag{147}$$

where now  $\hat{\phi}^n$  and  $\Delta \hat{\phi}$  are  $N_x^2$ -vectors with elements  $\hat{\phi}_p^n$  and  $\Delta \hat{\phi}_p$ , respectively, and  $\mathbf{I}$  is the identity matrix. The elements of the  $\mathbf{A}$  matrix are

$$A_{p-N_x, p} = \frac{\hat{m}_{j,k-1/2} \hat{D}_{j,k-1/2}^{n+1/2}}{\hat{m}_{j,k} h^2}, \tag{148}$$

$$A_{p-1, p} = \frac{\hat{m}_{j-1/2, k} \hat{D}_{j-1/2, k}^{n+1/2}}{\hat{m}_{j,k} h^2}, \tag{149}$$

$$A_{p+1, p} = \frac{\hat{m}_{j+1/2, k} \hat{D}_{j+1/2, k}^{n+1/2}}{\hat{m}_{j,k} h^2}, \tag{150}$$

$$A_{p+N_x, p} = \frac{\hat{m}_{j,k+1/2} \hat{D}_{j,k+1/2}^{n+1/2}}{\hat{m}_{j,k} h^2}, \tag{151}$$

$$A_{p, p} = -(A_{p-N_x, p} + A_{p-1, p} + A_{p+1, p} + A_{p+N_x, p}). \tag{152}$$

Note that the face values of the knot mass and mean diffusivity are obtained by linear interpolation, as in the 1D case, and that the diffusivity at the midpoint of the time interval is again obtained from an Adams–Bashforth extrapolation similar to (108).

### 3.6.1. Approximate factorization ADI

The bandwidth of the linear system (147) is approximately  $2N_x$ . We can reduce the bandwidth down to that of a tridiagonal system (effectively) by employing an approximate factorization Alternating Direction Implicit (ADI) method [10,39]. The approximate factorization is preferred over direct ADI because the extension of the method to 3D is still second-order in time.

We first rewrite (147) as

$$\left[ \mathbf{I} - \frac{\Delta t}{2} \mathbf{A}^x \right] \underbrace{\left[ \mathbf{I} - \frac{\Delta t}{2} \mathbf{A}'' \right]}_{\Delta \hat{\phi}^x} \Delta \hat{\phi} = [\Delta t \mathbf{A}] \hat{\phi}^n + \mathcal{O}(\Delta t^2), \tag{153}$$

where the elements of the  $\mathbf{A}^x$  matrix are

$$A_{p-1,p}^x = \frac{\hat{m}_{j-1/2,k} \widehat{D}_{j-1/2,k}^{n+1/2}}{\hat{m}_{j,k} h^2}, \tag{154}$$

$$A_{p+1,p}^x = \frac{\hat{m}_{j+1/2,k} \widehat{D}_{j+1/2,k}^{n+1/2}}{\hat{m}_{j,k} h^2}, \tag{155}$$

$$A_{p,p}^x = -\left( A_{p-1,p}^x + A_{p+1,p}^x \right), \tag{156}$$

and  $\mathbf{A}'' = \mathbf{A} - \mathbf{A}^x$ . Ignoring the  $\mathcal{O}(\Delta t^2)$  error, we then solve (153) for  $\Delta \hat{\phi}^x$ , which is merely the solution of a tridiagonal system,

$$\left[ \mathbf{I} - \frac{\Delta t}{2} \mathbf{A}^x \right] \Delta \hat{\phi}^x = [\Delta t \mathbf{A}] \hat{\phi}^n. \tag{157}$$

The key now is to reorder the lexicographical mapping. For the  $y$ -direction sweep we specify the solution vector index by

$$p' = (j - 1)N_y + k, \tag{158}$$

(note that  $N_y = N_x$  for our case) and define a new intermediate solution vector  $\Delta \hat{\phi}^y$  by the permutation  $\Delta \hat{\phi}_{p'}^y = \Delta \hat{\phi}_p^x$ . The mean shifts can now be computed by solving the tridiagonal system

$$\left[ \mathbf{I} - \frac{\Delta t}{2} \mathbf{A}^y \right] \Delta \hat{\phi} = \Delta \hat{\phi}^y, \tag{159}$$

where the elements of  $\mathbf{A}^y$  are

$$A_{p'-1,p'}^y = \frac{\hat{m}_{j,k-1/2} \widehat{D}_{j,k-1/2}^{n+1/2}}{\hat{m}_{j,k} h^2}, \tag{160}$$

$$A_{p'+1,p'}^y = \frac{\hat{m}_{j,k+1/2} \widehat{D}_{j,k+1/2}^{n+1/2}}{\hat{m}_{j,k} h^2}, \tag{161}$$

$$A_{p',p'}^y = -\left( A_{p'-1,p'}^y + A_{p'+1,p'}^y \right). \tag{162}$$

Note that the resulting solution vector from (159) maps back to the grid mean shifts by (158).

### 3.6.2. Detailed conservation, realizability and boundedness

Due to the finite-volume scheme, the interpolation scheme, and the decay-weighted CIC mean estimate, the conservation properties of the 2D implementation are identical to the 1D case.

Further, in analogy with (129), realizability is guaranteed by subtracting the species average mean shift from the FV mean shift at each knot. Let  $\Delta\hat{\phi}_{\alpha,jk}^{\text{FV}}$  be the result of the linear solve (159) for composition  $\alpha$ . The realizable mean shifts in the 2D case are given by

$$\Delta\hat{\phi}_{\alpha,jk} = \Delta\hat{\phi}_{\alpha,jk}^{\text{FV}} - \frac{1}{n_s} \sum_{\beta=1}^{n_s} \Delta\hat{\phi}_{\beta,jk}^{\text{FV}}. \quad (163)$$

The extension of (135) to 2D yields the following bound for the effective decay-factor,

$$\tilde{c}_{jk} \geq \tilde{c}_{jk}^{\min} \equiv \max_{(\alpha,q,r)} \left( \left[ \frac{\Delta\hat{\phi}_{\alpha,q,r}}{\phi_{\alpha,\min}^n - \hat{\phi}_{\alpha,q,r}^n} \right], \left[ \frac{\Delta\hat{\phi}_{\alpha,q,r}}{\phi_{\alpha,\max}^n - \hat{\phi}_{\alpha,q,r}^n} \right] \right), \quad (164)$$

for the knots  $(q, r) = \begin{bmatrix} (j-1, k+1) & (j, k+1) & (j+1, k+1) \\ (j-1, k) & (j, k) & (j+1, k) \\ (j-1, k-1) & (j, k-1) & (j+1, k-1) \end{bmatrix}$ .

Note that here we have included the composition index in the max operator of the decay-factor bound. Also, due to the bi-linear interpolation, the max must be taken over all the knots surrounding  $(j, k)$ .

#### 4. Test problems

In this section, we present a suite of test cases to demonstrate the properties of the new method for: (1) problems with constant and uniform fluid properties, (2) problems with variable diffusivity, (3) problems with composition fluctuations and potential boundedness violations, (4) problems with steep gradients in the scalar field, and (5) multi-dimensional problems.

As mentioned previously, the method assumes that the mean particle mass density remains constant over the course of a single time step. Hence, in practice this algorithm should be coupled into the overall particle solver in a fractional step in which the particle positions remain fixed. For the test cases considered here the particle mass density is taken to be uniform and constant and all particle positions are fixed throughout a given simulation. Particle positions are selected randomly from a uniform distribution within each cell. For the 1D problems, positions are then adjusted such that  $\hat{m}_j$  as defined by (106) is uniform. For the 2D problem, the positions are partially random (as is explained in Section 4.6) and laid down such that the knot masses are uniform without correction. The number of particles used for the quantitative convergence studies is large enough so that statistical errors are small relative to the bias in the kernel estimate.

The relevant dimensional parameters for a given test case are:

- $h$  the uniform grid spacing,
- $N_x$  the number of grid points in the domain in each direction,
- $N_c$  the number of particles per cell (uniform in all cases),
- $\Delta t$  the time step,
- $T$  the total time for the run,
- $D(\mathbf{x}, t)$  the diffusivity,
- $\omega(\mathbf{x}, t)$  the mixing rate,
- $f_{\phi|X}^*(\mathbf{x}, t_0)$  the initial distribution of particle compositions.

A table of parameters is given for each problem and, where necessary, the functional forms of the diffusivity, mixing rate, and initial scalar distribution are also specified.

##### 4.1. Problem 1: decay of a sine wave

###### 4.1.1. Definition of the problem

This is a simple problem designed to illustrate qualitative properties of the scheme in the DNS limit as well as to establish the spatial and temporal accuracy of the scheme for the case of constant and uniform diffusivity.

We take the diffusivity  $D$  to be unity. The 1D domain is periodic of length  $L = 2\pi$ . Recall that  $f_{\phi|X}^*$  is the PDF of particle composition conditional on particle position. We consider a sharp initial condition in the particle system given by the delta function

$$f_{\phi|X}^*(\psi; t_0|x) = \delta(\tilde{\phi}_0[x] - \psi), \tag{165}$$

where the initial mean is

$$\tilde{\phi}_0(x) = \alpha[1 + \sin(\gamma x)], \tag{166}$$

$\gamma = 2\pi/L = 1$ , and the amplitude is  $\alpha = 1/2$ , hence  $0 \leq \phi^* \leq 1$ . The particles are initialized by setting  $\phi^*(t_0) = \tilde{\phi}_0(X^*[t_0])$ .

The mean evolves by

$$\frac{\partial \tilde{\phi}}{\partial t} = D \frac{\partial^2 \tilde{\phi}}{\partial x^2}, \tag{167}$$

which has the solution

$$\tilde{\phi}(x, t) = \alpha[1 + \sin(\gamma x) \exp(-D\gamma^2 t)]. \tag{168}$$

The characteristic time scale for decay of the mean is defined as  $\tau \equiv (D\gamma^2)^{-1} = 1$ , so that the exponential in (168) can be written  $\exp(-t/\tau)$ . The normalized total time  $T/\tau$  for each simulation is shown in Table 2.

#### 4.1.2. Qualitative results

To illustrate the behavior of the method for a DNS application we specify a set of parameters for two cases, labeled Cases 1a and 1b (see Table 2). The first case shows resolution of the mode with four cells. Twice the spatial resolution with a larger time step is used for the second case. The normalized total time for the simulation,  $T/\tau$ , represents a single time step in each case. The results are shown in Figs. 4 and 5 for Cases 1a and 1b, respectively. As may be seen, even with the rather coarse resolution used ( $L/h = 4$  or  $8$ ,  $T/\tau = 1$  and  $N_c = 40$ ) the particle compositions agree quite well with the analytic solution, and no qualitatively unsatisfactory behavior is observed.

#### 4.1.3. Spatial convergence

The spatial convergence is examined by integrating (167) for a normalized total time of  $T/\tau = 1$  for a range of grid spacings ( $N_x = 8-64$ ) while holding the time step fixed at  $\Delta t/\tau = 0.001$ , which corresponds to a maximum Fourier number of  $Fo \equiv \Delta t D/h^2 \approx 0.1$  for the smallest grid spacing. In Fig. 6, we plot the infinity norm of the error, defined by

$$E_\infty(t) \equiv \max_j (|\hat{\phi}_j[t] - \tilde{\phi}[x_j, t]|), \tag{169}$$

Table 2  
Parameters for Problem 1

Case	Figure	$N_x$	$N_c$	$\omega\tau$	$Fo$
1a	Fig. 4	4	40	1	0.41
1b	Fig. 5	8	40	1	1.62
1c	Fig. 6	8–64	100	0.1	0.0016–0.10
1d	Fig. 6	8–64	100	1	0.0016–0.10
1e	Fig. 6	8–64	100	1.9	0.0016–0.10
1f	Fig. 6	8–64	100	10	0.0016–0.10
1g	Fig. 7	128	100	0.1	0.415–415
1h	Fig. 7	128	100	1	0.415–415
1i	Fig. 7	128	100	1.9	0.415–415
1j	Fig. 7	128	100	10	0.415–415

For this problem the domain is periodic of length  $L = 2\pi$ . The diffusivity is set to  $D = 1$ ; hence, the characteristic decay time scale is  $\tau = 1$ . The normalized total run time for each case is  $T/\tau = 1$ . The relevant figure for each case is listed in the second column followed by the number of grid cells,  $N_x$ ; the number of particles per cell,  $N_c$ ; the non-dimensional mixing rate,  $\omega\tau$ ; and lastly, the Fourier number,  $Fo \equiv \Delta t D/h^2$ .

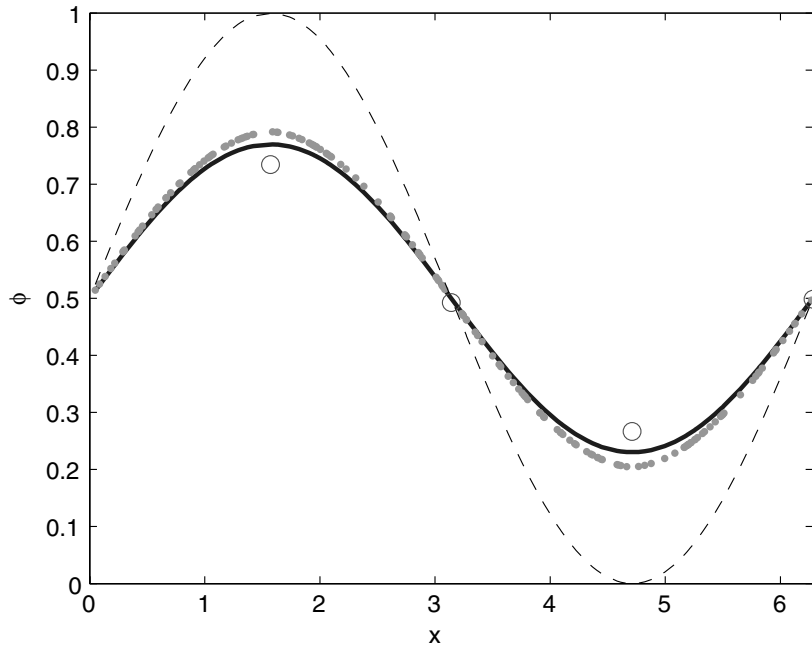


Fig. 4. (Case 1a) Decay of a sine wave on a 1D periodic domain of length  $L = 2\pi$  with  $D = 1$  and hence  $\tau = 1$ ;  $N_x = 4$ ,  $N_c = 40$ ,  $\omega\tau = 1$ ,  $Fo = 0.41$  and  $T/\tau = 1$ . The dashed line (---) is the initial condition for the mean  $\phi_0(x)$  given by (166). The particle compositions are initialized by setting  $\phi^*(0) = \tilde{\phi}_0(X^*)$ . The solid line (—) represents the exact solution (168) at time  $T/\tau = 1$ . The particle compositions are represented by the small gray dots (●) and the CIC means at the knot locations are represented by the open circles (○).

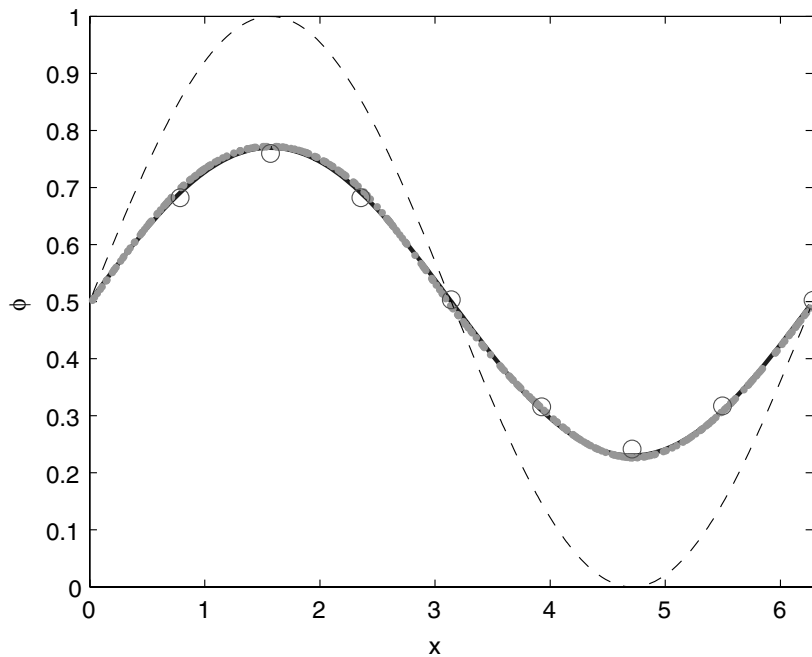


Fig. 5. (Case 1b) Decay of a sine wave on a 1D periodic domain of length  $L = 2\pi$  with  $D = 1$  and hence  $\tau = 1$ ;  $N_x = 8$ ,  $N_c = 40$ ,  $\omega\tau = 1$ ,  $Fo = 1.62$ , and  $T/\tau = 1$ . The dashed line (---) is the initial condition for the mean  $\phi_0(x)$  given by (166). The particle compositions are initialized by setting  $\phi^*(0) = \tilde{\phi}_0(X^*)$ . The solid line (—) represents the exact mean solution (168) at time  $T/\tau = 1$ . The particle compositions are represented by the small gray dots (●) and the CIC means at the knot locations are represented by the open circles (○). By comparing Fig. 4 and this figure, the spatial convergence of the scheme is clear.

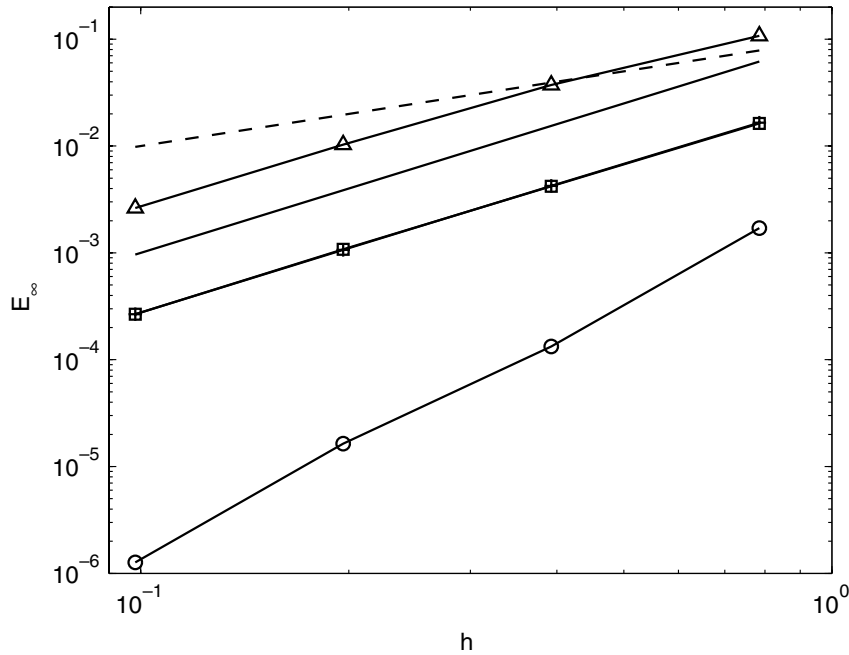


Fig. 6. Spatial convergence of the mean. The infinity norm of the error,  $E_\infty$ , defined by (169) is plotted against the grid spacing,  $h$ , for the sine wave decay problem (see Cases 1c–1f in Table 2). The dashed line (– –) represents first-order convergence and the thin solid line (—) represents second-order convergence. The connected symbols are simulation results for various values of the mixing rate: squares ( $\square$ )  $\omega\tau = 0.1$ , circles ( $\circ$ )  $\omega\tau = 1$ , plus (+)  $\omega\tau = 1.9$  and triangles ( $\triangle$ )  $\omega\tau = 10$ . The magnitude of the error depends nontrivially on the mixing rate. The convergence rate is  $\mathcal{O}(h^2)$  except when the value of the mixing rate causes a cancellation of errors, as in the  $\omega\tau = 1$  case, and then super-convergence is observed.

where  $\hat{\phi}_j(t)$  is obtained from (103) and  $\tilde{\phi}(x_j, t)$  is given by (168), against the grid spacing at  $t/\tau = 1$  for a range of mixing rates. There are four cases, labeled 1c–1f, corresponding to the different mixing rates used. The parameters for these cases are listed in Table 2. The spatial convergence of the scheme is generally second-order, except in special cases where a cancellation of errors leads to super-convergence of the solution, as explained below.

One should note that the error in the mean depends on the mixing rate even though the model for the mean (73) does not. This is a result of the bias error in the CIC mean estimate and is evident in the modified equation (138) (e.g. the fourth term on the RHS). The next thing to notice is that  $\omega$  has a nontrivial effect on the error: taking  $\omega\tau = 0.1$  as the first case with  $\tau$  constant, the error first decreases as  $\omega$  is increased, and then increases. This behavior can be understood by examining the modified equation in the limit of small  $\Delta t$ . First, however, we must recognize that the error we measure with (169) is based on a CIC mean and is biased. Thus, the error scales with the truncation error plus the measurement bias. With the solution given by (168), the fourth derivative of the mean can be related to the second derivative by

$$\frac{\partial^4 \tilde{\phi}}{\partial x^4} = -\gamma^2 \frac{\partial^2 \tilde{\phi}}{\partial x^2}. \tag{170}$$

Using (170), (169), (168), (138), (88) and (87), it can be shown that to leading order the observed error scales as

$$E_\infty \sim |1 + \omega T - 2D\gamma^2 T| h^2. \tag{171}$$

We can now understand the behavior of the convergence plot. Note that for this case we have  $1 + \omega T - 2D\gamma^2 T = \omega - 1$ . When the mixing rate is small compared to unity, as in Case 1c, the  $1 - 2D\gamma^2 T$  term dominates the error. In Case 1d, the mixing rate equals unity and so the coefficients cancel, leading to a smaller magnitude in the observed error and super-convergence of the solution (super-convergence also requires  $\omega = D$ , which, by considering (170), eliminates the  $\mathcal{O}(\Delta t h^2)$  error terms in the modified equation). In Case

ie, the mixing rate is larger than the  $1 - 2D\gamma^2$  term and the magnitude of the difference between  $\omega$  and unity is the same as in Case 1c. Thus, the magnitude of the observed error is identical. As the mixing rate is increased the first term dominates and the magnitude of the error increases, as in Case 1f. As mentioned, when the coefficients do not cancel, it is clear that the method is second-order accurate in space for this case.

4.1.4. Temporal convergence

The temporal convergence is examined by fixing the grid spacing and varying the time step. A range of mixing rates is tested for a fixed diffusivity. The parameters are listed as Cases 1g–1j in Table 2, and the results are plotted in Fig. 7. We use a small grid spacing so that we can examine large Fourier numbers. The results with  $Fo = 415$  further demonstrate the unconditional stability of the scheme. The error curves level off when the spatial error dominates. It is clear that the spatial error is controlling, even for large Fourier numbers. However, to the right of the plateau in each case the temporal convergence rate is consistent with the scheme being second-order accurate in time. For the special case of  $\omega = D = 1$  we again see that the leading error terms cancel, allowing the temporal convergence to continue to smaller Fourier numbers. It should be noted that the error plateau increases as  $\omega$  increases, as suggested by the modified equation for fixed  $h$ . Again, this issue is also present in the conventional approach of Anand and Pope [1].

4.2. Problem 2: decay of a sine wave with nonuniform diffusivity

4.2.1. Definition of the problem

This test problem is essentially the same as Problem 1, except that it is designed to establish the accuracy for the more relevant case of nonconstant and nonuniform diffusivity.

The mean composition evolves by

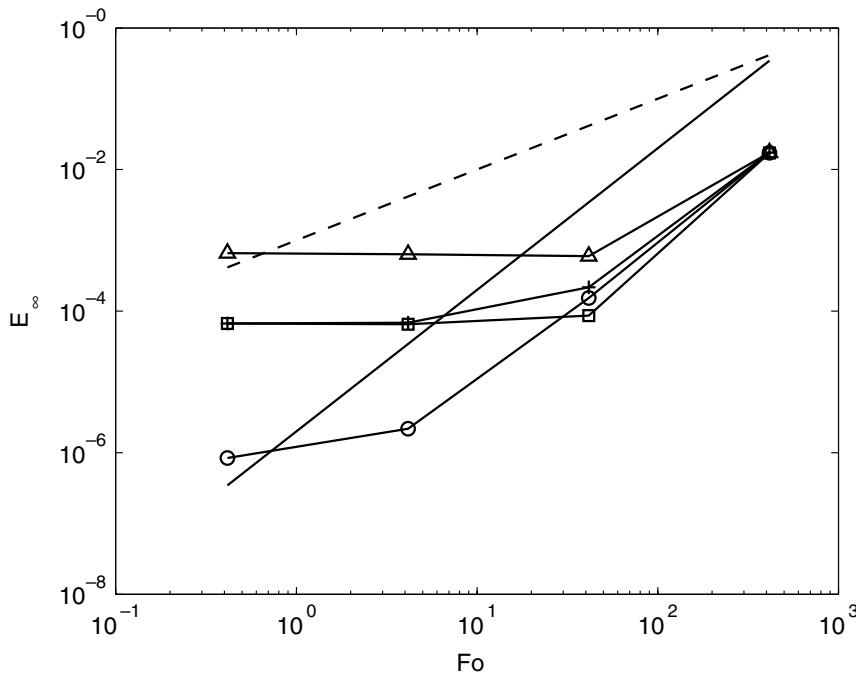


Fig. 7. Temporal convergence of the mean. The infinity norm of the error,  $E_\infty$ , defined by (169) is plotted against the Fourier number,  $Fo$ , for the sine wave decay problem (see Cases 1g–1j in Table 2). The grid spacing is held fixed. The dashed line (---) represents first-order convergence and the thin solid line (—) represents second-order convergence. The connected symbols are simulation results for various values of the mixing rate: squares ( $\square$ )  $\omega\tau = 0.1$ , circles ( $\circ$ )  $\omega\tau = 1$ , plus ( $+$ )  $\omega\tau = 1.9$  and triangles ( $\triangle$ )  $\omega\tau = 10$ . The curves plateau when the spatial error begins to dominate. As suggested by the modified equation (see Section 3.5.8), when  $h \leq \sqrt{\Delta t}$  the convergence rate is  $\mathcal{O}(\Delta t^2)$ .



$$\frac{\partial \tilde{\phi}}{\partial t} = \frac{\partial}{\partial x} \left( \tilde{D} \frac{\partial \tilde{\phi}}{\partial x} \right). \tag{172}$$

No analytical solution is presented. Instead we use Richardson extrapolation to assess the convergence rate. This is further discussed below. The initial condition for the mean is again specified by (166) and the composition PDF conditional on position is specified by (165), i.e. there are no fluctuations.

The diffusivity is defined to be proportional to the composition,

$$D(\phi^*[t]) = 0.1 + \phi^*(t). \tag{173}$$

The factor 0.1 is added to the diffusivity to prevent the formation of discontinuities in the solution at  $x = 3\pi/2$  where  $\tilde{\phi}$  is initially zero. The CIC estimate of the mean diffusivity at the knots is obtained using (107) and (173).

#### 4.2.2. Qualitative results

The parameters for this problem, reported in Table 3, are normalized based on a reference diffusivity  $D_{\text{ref}} = 1$ . The mixing rate is set proportional to the mean diffusivity and therefore also varies in space and time. The normalized total time for the simulation is set to  $T/\tau = 1$ , which is nominally the characteristic decay time scale. The refined numerical solution ( $N_x = 128$ ) is shown in Fig. 8 and serves to illustrate the form of the analytical solution for this case.

#### 4.2.3. Spatial convergence

The parameters for these spatial convergence tests are listed as Case 2b in Table 3, and the results are shown in Fig. 9. The error is obtained from Richardson extrapolation:

$$E_\infty(2h) = \max_j (|\hat{\phi}_j(2h) - \hat{\phi}_j(h)|), \tag{174}$$

where  $\hat{\phi}_j(2h)$  and  $\hat{\phi}_j(h)$  are the numerical solutions at location  $x_j$  based on a grids of width  $2h$  and  $h$ , respectively. Clearly,  $E_\infty$  varies as  $h^2$  (for small  $h$ ) demonstrating that the scheme is second-order accurate in space for this case with nonuniform diffusivity.

#### 4.2.4. Temporal convergence

The temporal convergence is assessed by first running a case with high spatial ( $N_x = 128$ ) and temporal resolution ( $\Delta t = 10^{-4}$ , nominally  $Fo = 0.04$ ) and treating the CIC means obtained from this run as the ‘‘converged solution’’,  $g_j$ . The infinity norm of the error for a coarser time step is then computed by

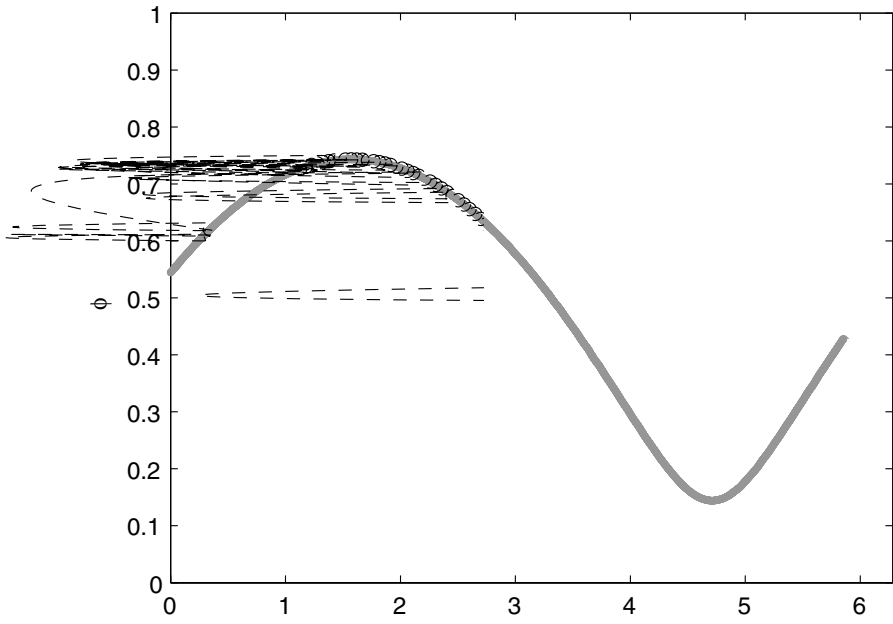
$$E_\infty(\Delta t) = \max_j (|\hat{\phi}_j(\Delta t) - g_j|). \tag{175}$$

The parameters for this series of runs is listed as 2c in Table 3, and the convergence plot is shown in Fig. 10. The convergence rate is second-order in time until the time step becomes  $\mathcal{O}(h^2)$ , which for this problem is  $h^2 \approx 0.002$ . At this point the  $\mathcal{O}(\Delta t h^2)$  terms and the  $\mathcal{O}(\Delta t^2)$  terms are comparable (see the modified equation (138)). Upon further reduction in the time step the  $\mathcal{O}(\Delta t h^2)$  term dominates the error and the convergence rate becomes first-order.

Table 3  
Parameters for Problem 2

Case	Figure	$N_x$	$N_c$	$\omega\tau$	$Fo$
2a	Fig. 8	128	100	$\tilde{D}(x, t)/D_{\text{ref}}$	0.4
2b	Fig. 9	8–64	100	$\tilde{D}(x, t)/D_{\text{ref}}$	0.002–0.1
2c	Fig. 10	128	100	$\tilde{D}(x, t)/D_{\text{ref}}$	0.4–400

In this problem the domain is periodic with length  $L = 2\pi$ . Quantities are non-dimensionalized based on the reference diffusivity  $D_{\text{ref}} = 1$ . Thus,  $\tau \equiv (D_{\text{ref}})^{-1} = 1$ . The normalized total time for all runs is  $T/\tau = 1$ . The local diffusivity is compute using (173). The relevant figure is listed in the second column followed by the number of grid cells,  $N_x$ ; the number of particles per cell,  $N_c$ ; the non-dimensional mixing rate,  $\omega\tau$  (a function of space and time for this problem); and lastly, the Fourier number,  $Fo \equiv \Delta t D_{\text{ref}}/h^2$ .



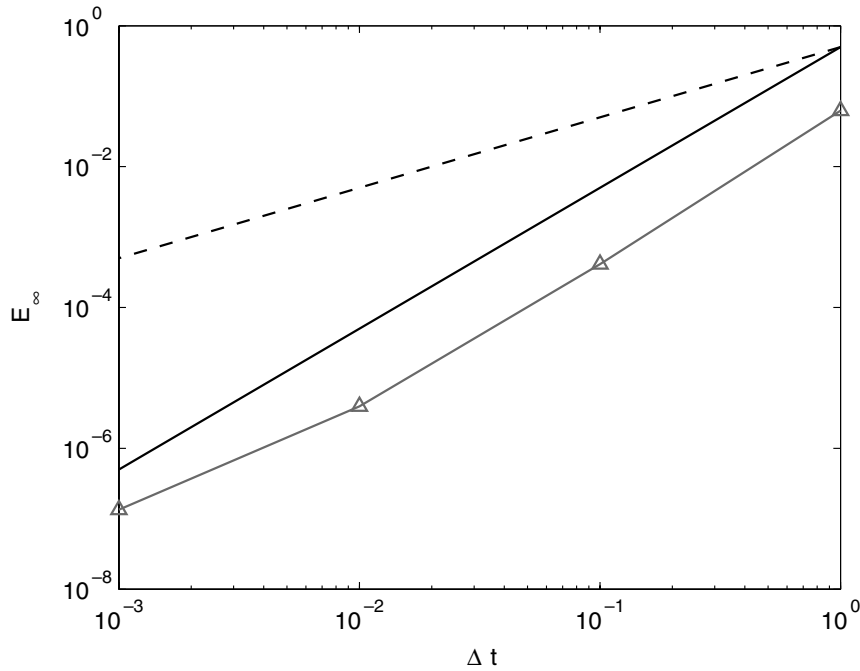


Fig. 10. Variable diffusivity temporal convergence study. The infinity norm of the error,  $E_\infty$ , defined by (175) is plotted against the time step,  $\Delta t$ , with fixed  $h$  for the case where the diffusivity is specified by (173). Parameters are listed as Case 2c in Table 3. The dashed line (– –) represents first-order convergence and the thin solid line (—) represents second-order convergence. The connected triangles ( $\Delta$ ) are the simulation results. The method is  $\mathcal{O}(\Delta t^2)$  accurate for this case until  $\Delta t \approx h^2$ , at which point the convergence rate becomes first-order in time in agreement with the modified equation (138).

### 4.3. Problem 3: decay of a sine wave with fluctuations

This problem is designed to illustrate the behavior of the scheme with regard to boundedness. As in Problem 1, here we take the diffusivity  $D$  to be unity and the 1D domain is periodic of length  $L = 2\pi$ . Recalling that  $f_{\phi|X}^*$  is the PDF of particle compositions conditional on particle position, we consider an initial distribution in the particle system which (for each position  $x$ ) is uniform in composition space. Specifically, at time  $t_0$  we have

$$f_{\phi|X}^*(\psi; t_0|x) = \begin{cases} \frac{1}{2\tilde{\phi}_0(x)} & \text{for } 0 \leq \psi \leq 2\tilde{\phi}_0(x), \\ 0 & \text{otherwise,} \end{cases} \tag{176}$$

where the initial mean is specified as

$$\tilde{\phi}_0(x) = \alpha[1 + \sin(\gamma x)], \tag{177}$$

where  $\gamma = 2\pi/L = 1$  and we set  $\alpha = 1/4$ ; thus  $2\tilde{\phi}_0(\pi/2) = 1$  and  $0 \leq \phi^* \leq 1$ . Hence, the characteristic time scale for decay of the mean is  $\tau \equiv (D\gamma^2)^{-1} = 1$ . After the particle position  $X^*$  has been initialized, the particle composition is initialized at random, uniformly in  $[0, 2\tilde{\phi}_0(X^*)]$ .

This problem is a stringent test of the boundedness constraints. Based on (176),  $\phi^* = 0$  is initially possible for all values of  $X^*$ . Consider an initial composition  $\phi^*(t_0) = 0$  with  $X^*$  anywhere in  $(0, \pi)$ . If the specified mixing rate is too low, i.e. if  $\omega(X^*, t_0) < \omega_{\min}(X^*, t_0)$  where  $\omega_{\min}$  is defined by (57) for a single composition, then the negative mean shift (due to the negative curvature of the sine function on  $(0, \pi)$ ) immediately causes the particle composition to violate the minimum bound.

To test the ability of the numerical method to satisfy boundedness for  $\omega = \omega_{\min}$  we specify a uniform mixing rate that varies in time such that, at the position of maximum (negative) mean shift, which occurs at  $x = \pi/2$  for this problem, a particle composition at the lower bound remains there. That is, if  $X^*(t_0) = \pi/2$  and  $\phi^*(t_0) = 0$ , then  $\phi^*(t)$  remains zero for all time. This critical mixing rate is determined from (168) and is given by

$$\omega(t) = [\omega_{\min}(x, t)]_{x=\frac{\pi}{2}, t} = \left[ \frac{\partial_t \tilde{\phi}}{\phi_{\min} - \tilde{\phi}} \right]_{x=\frac{\pi}{2}, t} = \left( \frac{e^{-t/\tau}}{1 + e^{-t/\tau}} \right) \tau^{-1}. \quad (178)$$

The mixing rate (178) is initially half the inverse of the mean decay time scale,  $\omega_0 \equiv \omega(t_0) = (2\tau)^{-1}$ , and decreases nonlinearly to zero at long times.

Case 3a is set up to test the ability of the numerical method to enforce the boundedness constraints for well-posed problems without adjustment of the decay-factor. The mixing rate is specified by (178) and we do not implement the decay-factor adjustment described in Step 1 of Algorithm 1.

The initial condition for Case 3a is shown in Fig. 11. Parameters for this case are specified in Table 4. As the mean evolves the particle compositions in  $(0, \pi/2)$  experience a negative shift. The particles near the boundary in composition space must mix toward the mean at a rate as fast as or faster than the negative mean shift to avoid a boundedness violation. The end result of the Case 3a simulation is shown in Fig. 12. Notice that the particles in the neighborhood of  $x = \pi/2$  still lie close to the initial lower composition boundary, confirming that the numerical method performs well for this case.

However, even though the final state is within the initial bounds, extremely small boundedness violations occurred during the course of the Case 3a simulation ( $\min(\phi^*)/\alpha \approx -0.004$ , recall that  $\alpha = 1/4$  is the initial mean amplitude). These excursions illustrate that, even though the model is bounded, the numerics can lead to boundedness violations and therefore in practice it is important to use the the decay-factor adjustment given in Step 1 of Algorithm 1, which enforces (135).

Case 3b is identical to Case 3a, except that the decay-factor adjustment is implemented (see Table 4). No boundedness violations occur and the resulting final compositions for this case, shown in Fig. 13, are nearly identical to the results shown in Fig. 12. This confirms that the adjustments are small. Due to the linear interpolation of the decay factors, small adjustments do not degrade the  $\mathcal{O}(h^2)$  accuracy of the scheme.

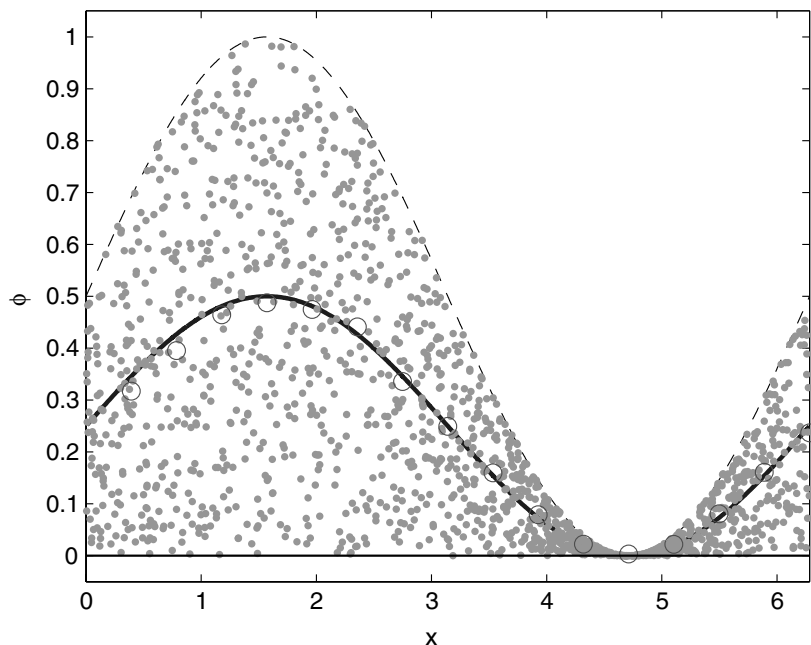


Fig. 11. Initial condition for Problem 3. The domain is periodic of length  $L = 2\pi$ . There are  $N_x = 16$  grid nodes and  $N_c = 40$  particles per cell. A full set of parameters is listed in Table 4. The particle compositions, represented by the gray dots ( $\bullet$ ), are initialized randomly from a uniform distribution with lower bound zero, marked by the thin line ( $-$ ), and an upper bound, shown by the dashed line ( $- -$ ), specified to be twice the exact mean, shown by the solid line ( $-$ ). The CIC means are represented by the open circles ( $\circ$ ).

Table 4  
Parameters for Problem 3

Case	Figures	$N_x$	$N_c$	$\omega\tau$	$\omega$
3a	Figs. 11 and 12	16	100	Eq. (178)	
3b	Figs. 11 and 13	16	100	Eq. (178)	

In this problem the domain is periodic with length  $L = 2\pi$  and the diffusivity is set to 1 for each run is  $T/\tau = 1$ . The relevant figures are listed in the second column followed by the number of particles per cell,  $N_c$ ; the non-dimensional mixing rate,  $\omega\tau$  (a function of time for this problem); and the parameter  $\omega$  indicates whether or not the decay-factor adjustment procedure (i.e. Step 1 of Algorithm 1) is used.

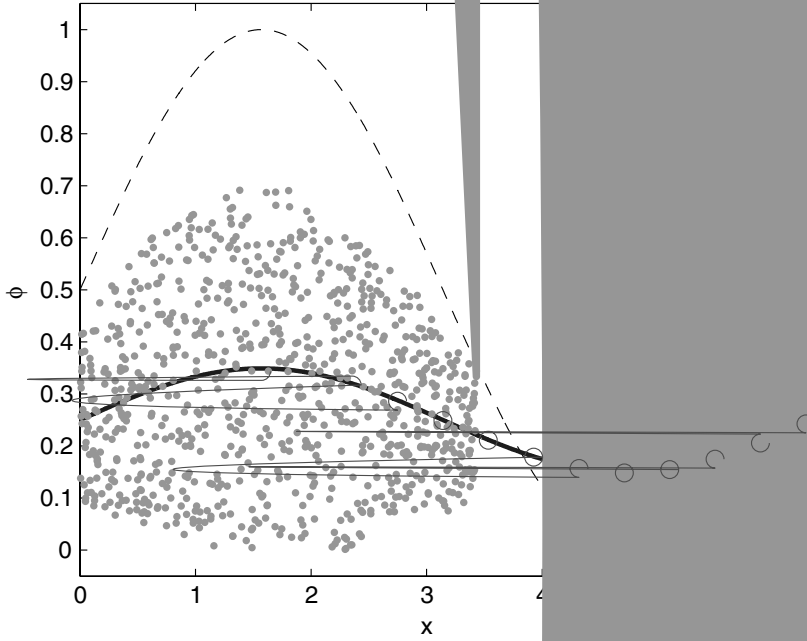


Fig. 12. Solution for Case 3a (no decay-factor adjustment). The initial lower bound of zero is marked by the thin line (—), the initial upper bound is marked by the dashed line (---), and the gray dots (•) represent the particles. The mixing rate is a function of time specified by (178) and for this problem is the minimum required for boundedness as dictated by (57). The maximum rate negative curvature occurs at  $x = \pi/2$ . For particles in this neighborhood, initial compositions close to zero remain near zero. Even though the final state is within the initial bounds, small boundedness violations are observed during the course of the simulation, confirming that a discrete adjustment is required, as discussed in Section 3.5.6. Notice that the CIC means, marked by the open circles (○), accurately match the analytical solution, denoted by the solid line (—).

#### 4.4. Problem 4: decay of the variance

This problem is designed to assess the temporal convergence for the problem definition is the same as Problem 3 in all respects, except that the definition of the mixing rate specified by (178) is ill-suited for determining the time error because it is only valid for the exponential decay weighting gives nearly perfect results, even for a large Fourier number. The result to show temporal convergence because the time error is insignificant. Because of this we use a prescribed function for the mixing rate:

$$\omega(t) = (\omega_0 - \lambda Tt + \lambda t^2), \quad (179)$$

where

$$\lambda \equiv -\frac{4(\omega_{\max} - \omega_0)}{T^2}. \quad (180)$$

The function (179) is parabolic with negative curvature. The initial and final mixing rates are both  $\omega_0$  and the maximum mixing rate,  $\omega_{\max}$ , is realized at  $t = T/2$  in the simulation. In the case presented below we set  $\omega_0 = 1/\tau$  and  $\omega_{\max} = 2/\tau$ .

Using the following transformation

$$s(t) \equiv 2 \int_0^t \omega(t') dt' = 2 \left[ \omega_0 t - \frac{1}{2} \lambda T t^2 + \frac{1}{3} \lambda t^3 \right], \tag{181}$$

it can be shown that the variance evolves by

$$\frac{d\tilde{Z}}{ds} = -\tilde{Z}, \tag{182}$$

with solution

$$\tilde{Z}(x, t) = \tilde{Z}_0(x) e^{-s}, \tag{183}$$

where, utilizing (176) and (177), the initial variance is given by

$$\tilde{Z}_0(x) \equiv \langle \phi^*(t_0)^2 | x \rangle - \langle \phi^*(t_0) | x \rangle^2 = \frac{(2\tilde{\phi}_0)^2}{12} = \frac{\alpha^2}{3} [1 + 2 \sin(\gamma x) + \sin^2(\gamma x)]. \tag{184}$$

The parameters for this case are listed in Table 5. The 1D domain is periodic with length  $L = 2\pi$  and the diffusivity is set to unity. The decay time scale for the mean is then  $\tau \equiv (D\gamma^2)^{-1} = 1$ . The normalized run time is kept short ( $T/\tau = 0.25$ ) because at long times the numerical solution approaches the trivial exact solution of zero variance. A large number of particles ( $N_c = 1000$ ) is used so that the initial CIC variance is close to the variance given by (184).

Table 5  
Parameters for Problem 4

Case	Figure	$N_x$	$N_c$	$\omega\tau$	$Fo$
4	Fig. 14	64	1000	Eq. (179)	3.2–26

In this problem the domain is periodic with length  $L = 2\pi$  and the diffusivity  $D$  is set to unity. Thus,  $\tau = (D\gamma^2)^{-1} = 1$ . The normalized total time for this run is  $T/\tau = 0.25$ . The relevant figure is listed in the second column followed by the number of grid cells,  $N_x$ ; the number of particles per cell,  $N_c$ ; the non-dimensional mixing rate,  $\omega\tau$  (a function of time for this problem); and the Fourier number,  $Fo \equiv \Delta t D/h^2$ .

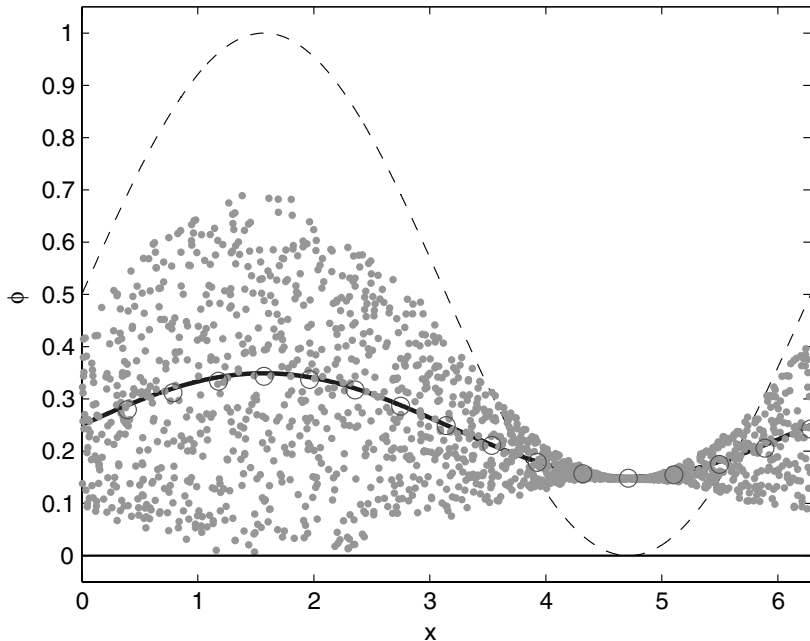


Fig. 13. Solution for Case 3b (with decay-factor adjustment). The initial lower bound of zero is marked by the thin line (—), the initial upper bound is marked by the dashed line (---) and the gray dots (●) represent the particles. The parameters for this run are listed as Case 3b in Table 4. The mixing rate is a function of time specified by (178) and for this problem is the minimum required for boundedness as dictated by (57). If the knot decay-factors determined from this mixing rate do not satisfy (135) for a given knot  $j$ , then we set  $\tilde{c}_j = \tilde{c}_j^{\min}$ . This is the “decay-factor adjustment procedure” given in Step 1 of Algorithm 1. With this procedure invoked, no boundedness violations can occur. By comparison with Fig. 12, we can see that the quality of the solution is not affected by this minor adjustment. Also, the CIC means, marked by the open circles (○), accurately match the analytical solution, denoted by the solid line (—).

To mitigate statistical errors when assessing the temporal convergence rate we compare the numerical solution against a solution that is initialized by the CIC variance. At a given time  $t$  the CIC variance is obtained from

$$\hat{Z}_j(t) = \frac{\sum_i B_j(X^{(i)}[t])m^{(i)}(\phi^{(i)}[t])^2}{\hat{m}_j} - \hat{\phi}_j^2(t). \tag{185}$$

The infinity norm of the error is then computed by

$$E_\infty(t) = \max_j (|\hat{Z}_j(t) - \hat{Z}_j(t_0) e^{-s(t)}|), \tag{186}$$

where  $s(t)$  is given by (181). In Fig. 14, we plot  $E_\infty(T)$  for a range of Fourier numbers showing that the convergence rate for the variance is second-order in time until spatial error due to the kernel estimation becomes significant.

#### 4.5. Problem 5: decay of a tophat function

This problem is meant to test the ability of the method to handle discontinuities in the composition field. Such situations arise in DNS near boundaries (e.g. a co-flow of fuel and air) and at flame fronts.

We consider the simple decay of a tophat function [7] with uniform and constant density, diffusivity, and mixing rate. As in Problem 1, the composition PDF conditional upon particle position is specified by the delta function (165). The domain for the analytical solution is infinite, but the computational domain is taken to be  $x \in [-\pi, \pi]$ , which is large enough to contain the significant nonzero values of the solution for the run time considered. Hence, for simplicity we use periodic boundaries in the computations. The half-width of the tophat function, which is symmetric about the origin, is given by the parameter  $H$ . The initial mean profile is then given by

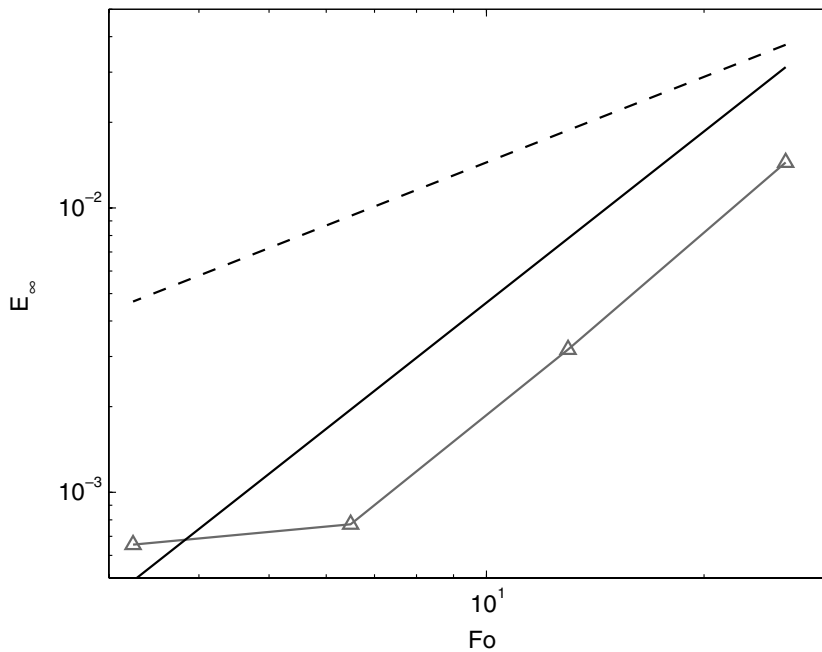


Fig. 14. Temporal convergence rate for the SGS variance. The parameters for this case are listed in Table 5. The particle compositions are initialized from the uniform distribution (176) and the mixing rate varies in time according to (179). Using a large number of particles per cell ( $N_c = 1000$ ) to minimize statistical error, the CIC variance is computed via (185). The error,  $E_\infty$ , defined by (186) is plotted against the Fourier number,  $Fo \equiv \Delta t D/h^2$ . The dashed line (– –) represents first-order convergence and the thin solid line (—) represents second-order convergence. The simulation data are shown by the connected triangles ( $\Delta$ ). As can be seen, the method is  $\mathcal{O}(\Delta t^2)$  accurate until the spatial error due to the CIC mean estimation becomes significant at small values of  $Fo$ .

$$\tilde{\phi}_0(x) = \begin{cases} 1 & \text{for } |x/H| \leq 1, \\ 0 & \text{otherwise.} \end{cases} \tag{187}$$

For  $t > 0$  the mean evolves by the error function solution

$$\tilde{\phi}(x, t) = \frac{1}{2} \tilde{\phi}_0(x) \left[ \operatorname{erf} \left( \frac{H-x}{2\sqrt{Dt}} \right) + \operatorname{erf} \left( \frac{H+x}{2\sqrt{Dt}} \right) \right]. \tag{188}$$

The diffusivity  $D$  is set to unity. The characteristic time scale for the decay of the square pulse – the time required for the peak to reach half its initial value – is given by  $\tau_H \equiv H^2/D$  [7]. This time scale, however, is ill-suited for representing the molecular mixing time scale across the discontinuity. The relevant length scale is the “width” of the discontinuity. In an LES, the resolution of the discontinuity is represented by the filter width  $\Delta$ . Here we will take  $\Delta = h$  and thus define the relevant mixing time scale as  $\tau_h \equiv h^2/D$ . For this problem we then set the non-dimensional mixing frequency  $\omega\tau_h$  to unity.

The particle compositions are initialized by setting  $\phi^*(t_0) = \tilde{\phi}_0(X^*[t_0])$  as shown in Fig. 15. Two cases are presented and their parameters are listed in Table 6. Each case is run to a normalized total time of  $T/\tau_H = 1/4$  using  $Fo = 1$ . The first case uses the method developed in this paper. For comparison the second case is run using the random walk/IEM approach as implemented by Jenny et al. [17]. The resulting profiles are shown in Figs. 16 and 17, respectively. The mean composition profiles are of comparable accuracy. However, as previously mentioned, the random walk/IEM method produces a spurious variance, which causes the particle compositions to deviate from the mean and renders the method unsuitable for use in DNS.

#### 4.6. Problem 6: decay of sinusoidal waves with fluctuations in 2D

The purpose of this problem is to verify the 2D formulation with regard to mean transport and boundedness. The 2D periodic domain is square with side  $L = 2\pi$ . We consider constant and uniform diffusivity with  $D = 1$  and test the discrete bound (164) by setting the mixing rate to be small, thus forcing the decay-factor adjustment procedure (analogous to Step 1 of Algorithm 1) to be invoked continuously.

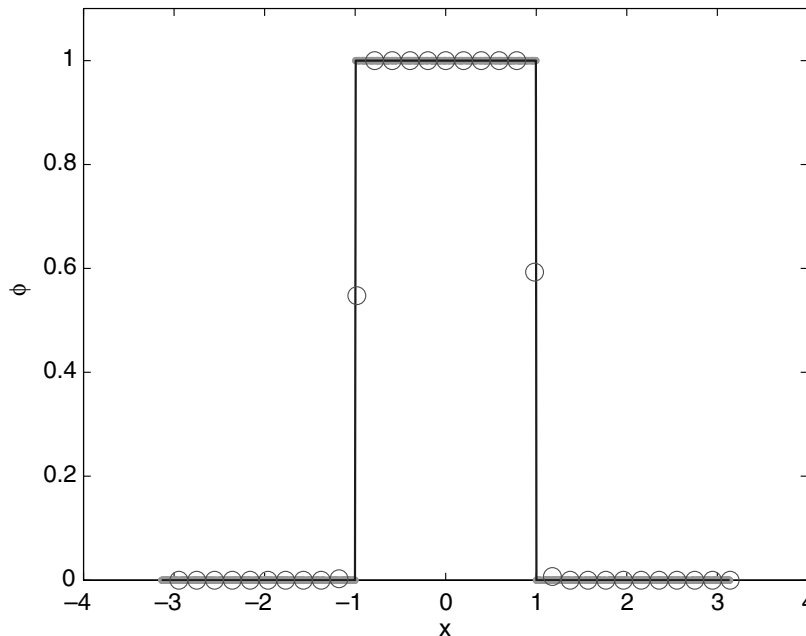


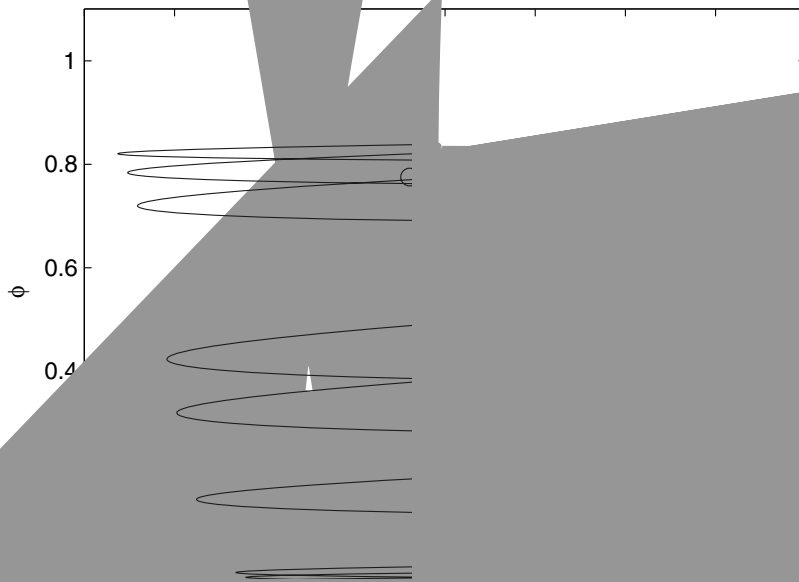
Fig. 15. Initial condition for Problem 5 – decay of a tophat function. The parameters for this case are listed in Table 6. The solid line (—) represents the initial condition for the mean (187). The particle compositions, represented by the gray dots (●), are initialized to the mean at their respective locations. The CIC means are marked by the open circles (○).



Table 6  
Parameters for Problem 5

Case	Figures	Method
5a	Figs. 15 and 16	New particle diffusion
5b	Figs. 15 and 17	Random walk/IEM

The computational domain is  $x \in [-\pi, \pi]$ . Homogeneous Dirichlet boundaries are used in the computation. The initial conditions are uniform over the domain. The diffusion coefficient  $D$  is set to unity. The time scale is given by  $\tau_H \equiv H^2/D = 1$  and the mixing time scale is given by  $\tau_m \equiv \omega^{-1} = 1$ . The normalized run time for each case is  $t = \tau_H \tau_m$ . The relevant figures are listed in the second column. The number of grid cells,  $N_x$ ; the number of particles per cell,  $N_p$ ; the dimensional mixing rate,  $\omega \tau_H$ ; and the Fourier number,  $\tau_H/D$ .



and  
particle  
distribution

This problem is a special case of the general problem. The initial conditions are uniform between the boundaries. The initial mean is of unity. The distribution is given by

$$f_{\phi|x,y}^*(\psi; t_0|x,y) = \begin{cases} \frac{1}{2\tilde{\phi}_0(x,y)} & \text{for } 0 \leq \psi \leq 2\tilde{\phi}_0(x,y) \\ 0 & \text{otherwise,} \end{cases}$$

where the initial mean is specified by

$$\tilde{\phi}_0(x, y) = \alpha \left( 1 + \left[ \frac{1}{2} \sin(\gamma x) + \frac{1}{2} \sin(\gamma y) \right] \right), \tag{190}$$

with  $\gamma = 2\pi/L = 1$  and  $\alpha = 1/4$ ; thus  $2\tilde{\phi}_0(\pi/2, \pi/2) = 1$  and  $0 \leq \phi^* \leq 1$ . The characteristic time scale for decay of the mean is  $\tau \equiv (D\gamma^2)^{-1} = 1$ . The mean evolves by the simple heat equation

$$\frac{\partial \tilde{\phi}}{\partial t} = D\nabla^2 \tilde{\phi}. \tag{191}$$

With the initial condition given by (190), the analytical solution to (191) is

$$\tilde{\phi}(x, y, t) = \alpha \left( 1 + \left[ \frac{1}{2} \sin(\gamma x) + \frac{1}{2} \sin(\gamma y) \right] \exp\{-t/\tau\} \right). \tag{192}$$

The parameters for Problem 6 are given in Table 7. The grid is square with  $N_x = 16$  nodes in each direction. The number of particles per cell we use,  $N_c = 40$ , is typical of FDF computations [13]. The specified mixing

Table 7  
Parameters for Problem 6

Case	Figures	$N_x$	$N_c$	Specified $\omega\tau$	$Fo$
6	Figs. 18–20	16	40	$\ll \omega_{\min}\tau$	1

The 2D periodic domain is square with side  $L = 2\pi$ . The diffusivity is constant and uniform at  $D = 1$  and hence the characteristic decay time scale is  $\tau \equiv (D\gamma^2)^{-1} = 1$ . The simulation is run for a total normalized time of  $T/\tau = 1$ . The relevant figures are listed in the second column followed by the number of grid cells,  $N_x$ ; the number of particles per cell,  $N_c$ ; the non-dimensional mixing rate,  $\omega\tau$ ; and the Fourier number,  $Fo \equiv \Delta t D/h^2$ .

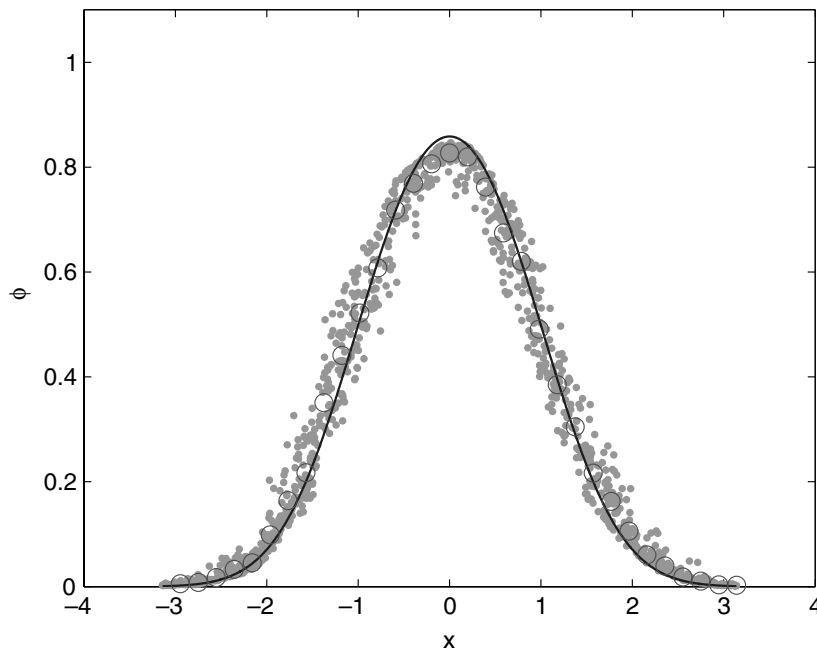
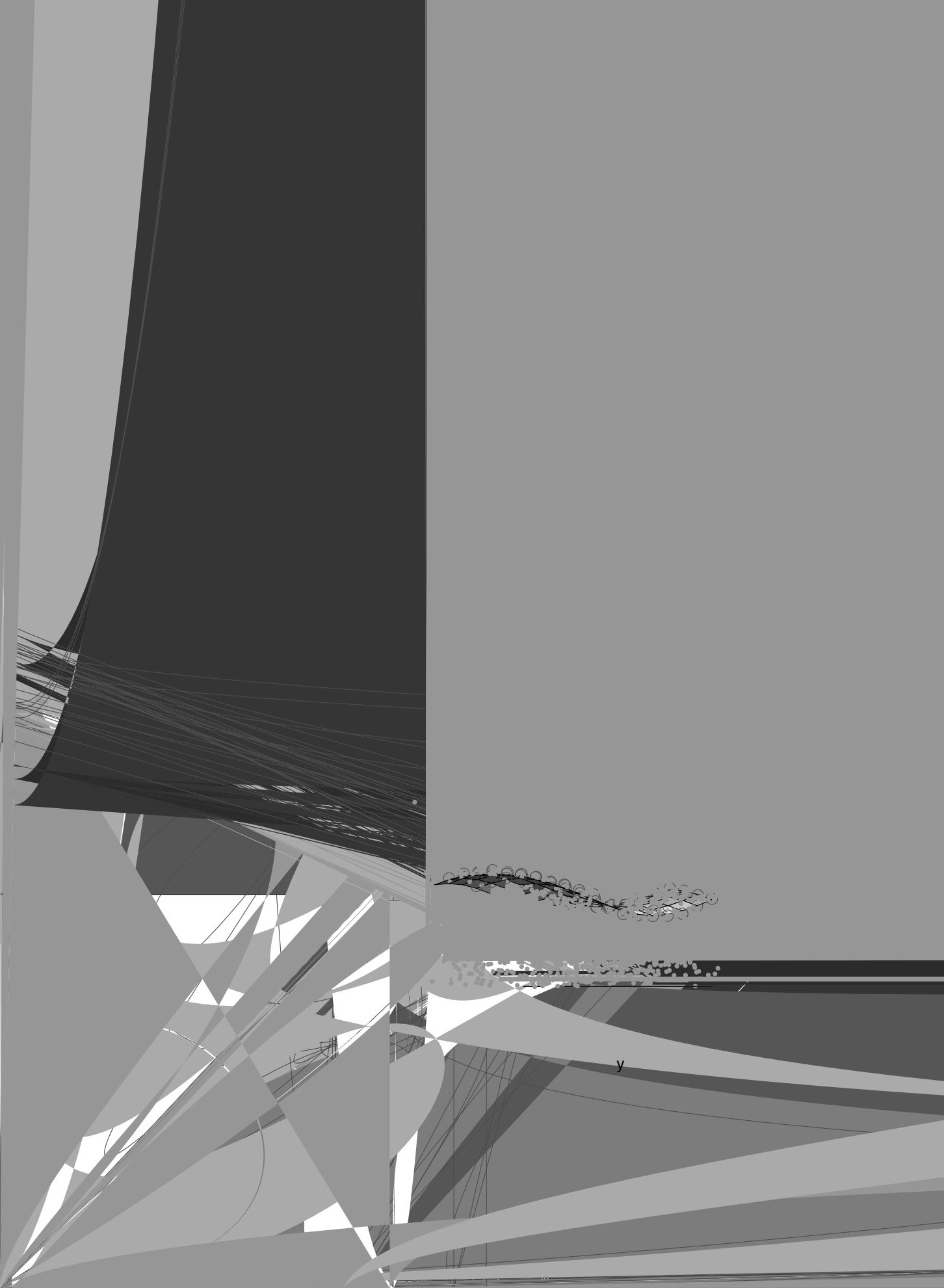


Fig. 17. Problem 5 solution using the random walk/IEM method of Jenny et al. [17]. The parameters are listed as Case 5b in Table 6. The simulation is run for 1/4 of the characteristic decay time scale of the square wave in order to keep the significant nonzero values of the solution within the computational domain. The analytical solution (188) is shown by the solid line (—). The particle compositions are represented by the gray dots (●) and the CIC means are marked by the open circles (○). As can be seen, the random walk transport model generates a spurious variance: even though the CIC means are in good agreement with the analytical solution, the individual particle compositions are in error. This behavior makes the random walk model ill suited for use in DNS.



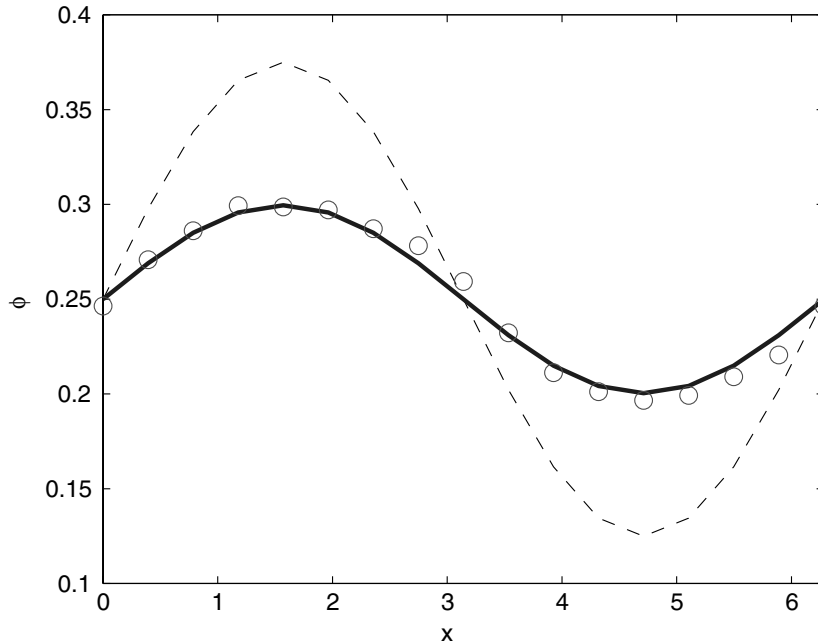


Fig. 20. Solution for Problem 6 – 1D slice. For the same case described in Fig. 19 above, the CIC means – shown by the open circles (○) – are plotted along a line in the  $x$  direction which crosses the  $y$  axis at the origin. The initial exact mean along this line is represented by the dashed line (---) and the analytical solution along this line is shown by the solid line (—). As can be seen, the agreement between the exact and CIC means is satisfactory.

rate is set to be much smaller than the minimum dictated by (57), thus forcing the decay-factor adjustment to be invoked continuously across the entire domain.

The simulation is run for a normalized total time of  $T/\tau = 1$  using  $Fo = 1$ . The initial condition is shown in Fig. 18. The final state of the run is shown in Fig. 19 where the plot is oriented to show that the compositions remain bounded. Since everywhere we have  $\tilde{c}_{jk} = \tilde{c}_{jk}^{\min}$  as given by (164), particles initially close to the lower boundary remain there. These results are a testament to the robustness of the adjustment procedure. To provide a better view of the mean result, in Fig. 20, we plot the CIC means and the mean exact solution along the  $x$  direction for  $y = 0$  at time  $T/\tau$ . These results confirm that the new method is easily extended to – and works well in – multi-dimensions.

## 5. Conclusions

The key contributions of this paper are:

- (1) the introduction of a new molecular diffusion model for the FMDF equation (51) and a corresponding particle formulation (Eqs. (67), (75) and (77)), and
- (2) the development of a numerical method to solve the particle composition evolution equation (75).

The models for the continuous and particle systems (i.e. Eqs. (51) and (77), respectively) share the following properties:

- (i) The models account for spatial transport of the mean of the FMDF and the particle MDF.
- (ii) The models cause the SGS covariance to decrease and the equations reduce to the governing transport equations for DNS in the limit of vanishing filter width.
- (iii) Realizability is obeyed for the diffusion velocity-corrected forms of the models and individual boundedness is obeyed for well-posed problems (i.e. problems where the mixing rate satisfies (57)).

- (iv) Linearity and independence principles are obeyed for the case of equal diffusivities.
- (v) The models can account for differential diffusion at length scales equal to or greater than the filter width.
- (vi) The influence of reaction on mixing could be accounted for through a Damköhler-number dependence on the mixing rate, but this issue is not addressed here.
- (vii) The models are amenable to solution via an efficient particle method as has been developed herein.

Details of the numerical method for solving the particle composition evolution equation (75) are outlined in Algorithm 1 in Section 3. The properties of the scheme are:

- (a) The scheme is consistent, second-order accurate in space, and second-order accurate in time under the condition that the spatial truncation error is not dominant (i.e. the temporal convergence rate is  $\mathcal{O}(\Delta t^2)$  provided that  $h^2/\Delta t$  remains bounded as  $\Delta t$  tends to zero).
- (b) The scheme ensures detailed conservation.
- (c) The scheme ensures realizability and individual boundedness of the compositions.
- (d) The scheme is unconditionally stable.
- (e) The particle-based cost scales linearly with the number of particles and the number of compositions (with the possible exception of evaluating the diffusion coefficient), and for typical combustion calculations this cost dominates over the grid-based cost.

The conventional approach for treating the unclosed molecular diffusion term accounts for spatial transport through a random walk in the particle position equation (see Section 2.8). There are two significant shortcomings to this approach which are overcome by our new method. First, the composition variance equation for the random walk model contains a spurious (i.e. nonphysical) production term and hence this formulation induces fluctuations to the solution, even if the flow field is well resolved. Therefore, one does not attain a DNS solution in the limit of vanishing filter width. The second shortcoming of the random walk approach is that, because all particles disperse according to a single diffusion coefficient in the position equation, the model cannot account for differential diffusion.

In our new approach spatial transport due to molecular diffusion is modeled by a mean drift term in the particle composition equation (75). This allows differential diffusion to be handled easily. Because there is no random walk in the position equation, no spurious fluctuations are introduced, and thus the method is well suited for DNS. One disadvantage of the new method is that molecular transport of the variance is ignored. However, this is a common assumption made in modeling high-Reynolds-number flows since turbulent transport typically dominates when the variance is significant.

Within this work we have established the formal correspondence between the models for the FMDF (45) and the Lagrangian particle MDF (72) (the diffusion velocity-corrected forms of the models (51) and (77), likewise correspond). It is shown that the filtered mass density from the continuous system is proportional to the marginal PDF of particle position, with the proportionality coefficient being the total system mass. It is also shown that the Favre-filtered fields in the continuous system correspond to the mean fields in the particle system conditional upon the particle position. For constant system mass, the model FMDF and model Lagrangian particle MDF transport equations immediately correspond, and it follows that all moment equations also correspond. Thus, with the appropriate initial and boundary conditions, a solution to the model particle MDF equation is equivalent to the solution of the corresponding model FMDF equation.

Another important aspect of molecular diffusion is mixing in composition space, which causes decay of the scalar variance. In our approach we employ the simple IEM mixing model. Both the new FMDF model (51) and the new particle MDF model (77) share the important characteristic that individual boundedness constraints on the compositions imply a minimum bound (57) on the mixing frequency used in the IEM model. We require that the mixing frequency satisfy this bound in order to form a well-posed problem. However, we demonstrate that small adjustments may be necessary in order to guarantee boundedness of the numerical solution. We also provide the exact form required for these adjustments in 1D (135) and in 2D (164).

Note that the method developed here can be used with other mixing models (e.g. the modified Curl (MC) mixing model [8] or the Euclidean minimum spanning tree (EMST) mixing model [38]) as follows: with  $\omega \geq \omega_{\min}$  as required for a well-posed problem by the mixing rate bound (57), in the mixing substeps, perform

IEM with  $\omega = \omega_{\min}$ , then use the other mixing model with rate  $(\omega - \omega_{\min})$ . All model properties (including individual boundedness) are still guaranteed.

In addition to the theoretical framework described above, we develop a numerical method to solve the particle composition equation (75) that is second-order accurate in space and time, obeys detailed conservation, ensures boundedness of the compositions, and is unconditionally stable. Details of the method are outlined in Algorithm 1. The scheme is a Strang-splitting approach that takes half an IEM step in the first stage, a full transport step in the second stage, and another half IEM step in the final stage. The scheme is unconditionally stable by virtue of an analytic solution for the IEM steps and a Crank–Nicolson scheme for the transport step. Second-order accuracy in space is achieved through a standard finite-volume method for the mean transport and a symmetric kernel estimator for the CIC mean. Second-order accuracy in time is achieved due to the Strang-splitting and Crank–Nicolson methods. Note that any other stable and accurate scheme for solving the diffusion equation can be used in the transport substep. Thus, the general framework of the scheme (i.e. the Strang-splitting, CIC mean estimation, linear interpolation, realizability correction to mean shift, and boundedness adjustment procedure) can be extended to unstructured grids. However, caution must be exercised because second-order spatial accuracy for the overall scheme requires symmetry of the kernel in the CIC mean estimate.

Finally, we derive a modified equation (136) for the scheme which shows that numerical diffusion terms exist which are proportional to the IEM mixing rate. This numerical diffusion arises due to the bias error in the IEM steps and is also present in the numerical schemes used in the conventional random walk/IEM approach.

## Acknowledgements

This research was supported by the National Science Foundation through Grant CBET-0426787. The authors would like to thank Zhuyin Ren for helpful discussions.

## References

- [1] M.S. Anand, S.B. Pope, Diffusion behind a line source in grid turbulence, in: L.J.S. Bradbury et al. (Eds.), *Turbulent Shear Flows*, vol. 4, Springer-Verlag, Berlin, 1985, pp. 46–61.
- [2] J.D. Anderson Jr., *Computational Fluid Dynamics: The Basics with Applications*, McGraw-Hill, 1995.
- [3] R.W. Bilger, Molecular transport effects in turbulent diffusion flames at moderate Reynolds numbers, *AIAA J.* 20 (7) (1982) 962–970.
- [4] R.B. Bird, W.E. Stewart, E.N. Lightfoot, *Transport Phenomena*, John Wiley and Sons, 1960.
- [5] F. Bisetti, J.Y. Chen, Numerical issues of Monte Carlo PDF for large eddy simulations of turbulent flames, Technical Report BisettiJUSS05, University of California, Berkeley, 2005.
- [6] P.J. Colucci, F.A. Jaber, P. Givi, Filtered density function for large eddy simulation of turbulent reactive flows, *Phys. Fluids* 10 (2) (1998) 499–515.
- [7] J. Crank, *The Mathematics of Diffusion*, second ed., Oxford University Press, 1975.
- [8] R.L. Curl, Dispersed phase mixing. I. Theory and effects in simple reactors, *AIChE J.* 9 (1963) 175–181.
- [9] C. Dopazo, E.E. O'Brien, Approach to autoignition of a turbulent mixture, *Acta Astronaut.* 1 (1974) 1239–1266.
- [10] J. Douglas, J.E. Gunn, A general formulation of alternating direction methods – Part I. Parabolic and hyperbolic problems, *Numer. Math.* 6 (1964) 428–453.
- [11] R.O. Fox, *Computational Models for Turbulent Reacting Flows*, Cambridge, 2003.
- [12] F. Gao, E.E. O'Brien, A large-eddy simulation scheme for turbulent reacting flows, *Phys. Fluids A* 5 (1993) 1282.
- [13] L.Y.M. Gicquel, P. Givi, F.A. Jaber, S.B. Pope, Velocity filtered density function for large eddy simulation of turbulent flows, *Phys. Fluids* 14 (3) (2002) 1196–1213.
- [14] P. Givi, Filtered density function for subgrid scale modeling of turbulent combustion, *AIAA J.* 44 (1) (2006) 16–23.
- [15] M.T. Heath, *Scientific Computing: An Introductory Survey*, second ed., McGraw-Hill, 2002.
- [16] F.A. Jaber, P.J. Colucci, S. James, P. Givi, S.B. Pope, Filtered mass density function for large-eddy simulation of turbulent reacting flows, *J. Fluid Mech.* 401 (1999) 85–121.
- [17] P. Jenny, S.B. Pope, M. Muradoglu, D.A. Caughey, A hybrid algorithm for the joint PDF equation of turbulent reactive flows, *J. Comp. Phys.* 166 (2001) 218–252.
- [18] A. Leonard, Large-eddy simulation of chaotic advection and beyond, *AIAA Paper* (97-0204), 1997.
- [19] R.P. Lindstedt, H.C. Ozarovskiy, R.S. Barlow, A.N. Karpetis, Progression of localized extinction in high Reynolds number turbulent jet flames, *Proc. Comb. Inst.* 31 (2007) 1459–1466.

- [20] A.K. Lohar, B.L. Sawford, Micromixing modelling of concentration fluctuations in inhomogeneous turbulence in the convective boundary layer, *Bound. Layer Meteorol.* 114 (2005) 1–30.
- [21] M. Pino Martín, U. Piomelli, G. Candler, Subgrid-scale models for compressible large-eddy simulations, *Theor. Comput. Fluid Dynam.* 13 (2000) 361–376.
- [22] P.A. McMurtry, S. Menon, A.R. Kerstein, A linear eddy subgrid model for turbulent reacting flows: application to hydrogen-air combustion, in: *Proceedings of the Comb. Inst.*, vol. 24, 1992, pp. 271–278.
- [23] M. Muradoglu, S.B. Pope, D.A. Caughey, The hybrid method for the PDF equations of turbulent reactive flows: consistency conditions and correction algorithms, *J. Comp. Phys.* 172 (2001) 841–878.
- [24] J.C. Oefelein, Simulation and analysis of turbulent multiphase combustion processes at high pressures, Ph.D. Thesis, The Pennsylvania State University, 1997.
- [25] N. Peters, *Turbulent Combustion*, Cambridge, 2000.
- [26] T. Poinso, D. Veynante, *Theoretical and Numerical Combustion*, second ed., Edwards, 2005.
- [27] S.B. Pope, Consistent modeling of scalars in turbulent flows, *Phys. Fluids* 26 (1983) 404–408.
- [28] S.B. Pope, PDF methods for turbulent reactive flows, *Prog. Energy Combust. Sci.* 11 (1985) 119–192.
- [29] S.B. Pope, Computations of turbulent combustion: progress and challenges, in: *Proceedings of the Comb. Inst.*, vol. 30, 1990, pp. 591–612.
- [30] S.B. Pope, *Turbulent Flows*, Cambridge, 2000.
- [31] S.B. Pope, M.S. Anand, Flamelet and distributed combustion in premixed turbulent flames, in: *Proceedings of the Comb. Inst.*, vol. 20, 1985, pp. 403–410.
- [32] V. Raman, H. Pitsch, A consistent LES/filtered-density function formulation for the simulation of turbulent flames with detailed chemistry, *Proc. Comb. Inst.* 31 (2007) 1711–1719.
- [33] V. Raman, H. Pitsch, R.O. Fox, Hybrid large-eddy simulation/Lagrangian filtered-density function approach for simulating turbulent combustion, *Combust. Flame* 143 (2005) 56–78.
- [34] M.R.H. Sheikhi, T.G. Drozda, P. Givi, F.A. Jaber, S.B. Pope, Large eddy simulation of a turbulent nonpremixed piloted methane jet flame (Sandia Flame D), in: *Proceedings of the Comb. Inst.*, vol. 30, 2005, pp. 549–556.
- [35] M.R.H. Sheikhi, T.G. Drozda, P. Givi, S.B. Pope, Velocity-scalar filtered density function for large eddy simulation of turbulent flows, *Phys. Fluids* 15 (2003) 2321–2337.
- [36] M.R.H. Sheikhi, P. Givi, S.B. Pope, Velocity-scalar filtered mass density function for large eddy simulation of turbulent reacting flows, *Phys. Fluids*, submitted for publication.
- [37] S. Subramaniam, Minimum error Fickian diffusion coefficients for mass diffusion in multicomponent gas mixtures, *J. Non-Equilib. Thermodyn.* 24 (1999) 1–39.
- [38] S. Subramaniam, S.B. Pope, A mixing model for turbulent reactive flows based on Euclidean minimum spanning trees, *Combust. Flame* 115 (1998) 487–514.
- [39] J.C. Tannehill, D.A. Anderson, R.H. Pletcher, *Computational Fluid Mechanics and Heat Transfer*, second ed., Taylor and Francis, 1997.
- [40] G.I. Taylor, Diffusion by continuous movements, in: *Proceedings of the Lond. Math. Soc.*, vol. 20, 1921, pp. 196–212.
- [41] R. Taylor, R. Krishna, *Multicomponent Mass Transfer*, John Wiley and Sons Inc., 1993.
- [42] S.R. Turns, *An Introduction to Combustion*, second ed., McGraw-Hill Higher Education, 2000.
- [43] J. Villermaux, J.C. Devillon, in: *Proceedings of the Second International Symposium on Chemical Reaction Engineering*, Elsevier, New York, 1972, pp. 1–13.